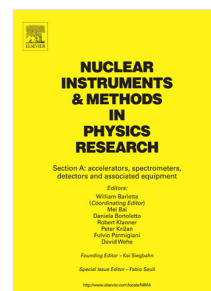


# Accepted Manuscript

The network of photodetectors and diode lasers of the CMS Link alignment system

P. Arce, J.M. Barcala, E. Calvo, A. Ferrando, M.I. Josa, A. Molinero, J. Navarrete, J.C. Oller, J. Brochero, A. Calderón, M.G. Fernández, G. Gómez, F.J. González-Sánchez, C. Martínez-Rivero, F. Matorras, T. Rodrigo, P. Ruiz-Árbol, L. Scodellaro, M. Sobrón, I. Vila, A.L. Virto, J. Fernández, P. Raics, Zs. Szabó, Z. Trócsnyi, B. Ujvári, Gy. Zilizi, N. Béni, G. Christian, J. Imrek, J. Molnar, D. Novak, J. Pálinkás, G. Székely, Z. Szillási, G.L. Bencze, G. Vestergombi, M. Benettoni, F. Gasparini, F. Montecassiano, M. Rampazzo, M. Zago, A. Benvenuti, H. Reithler, C. Jiang



PII: S0168-9002(18)30478-9  
DOI: <https://doi.org/10.1016/j.nima.2018.04.004>  
Reference: NIMA 60724

To appear in: *Nuclear Inst. and Methods in Physics Research, A*

Received date : 10 January 2018  
Revised date : 12 March 2018  
Accepted date : 4 April 2018

Please cite this article as: P. Arce, J.M. Barcala, E. Calvo, A. Ferrando, M.I. Josa, A. Molinero, J. Navarrete, J.C. Oller, J. Brochero, A. Calderón, M.G. Fernández, G. Gómez, F.J. González-Sánchez, C. Martínez-Rivero, F. Matorras, T. Rodrigo, P. Ruiz-Árbol, L. Scodellaro, M. Sobrón, I. Vila, A.L. Virto, J. Fernández, P. Raics, Z. Szabó, Z. Trócsnyi, B. Ujvári, G. Zilizi, N. Béni, G. Christian, J. Imrek, J. Molnar, D. Novak, J. Pálinkás, G. Székely, Z. Szillási, G.L. Bencze, G. Vestergombi, M. Benettoni, F. Gasparini, F. Montecassiano, M. Rampazzo, M. Zago, A. Benvenuti, H. Reithler, C. Jiang, The network of photodetectors and diode lasers of the CMS Link alignment system, *Nuclear Inst. and Methods in Physics Research, A* (2018), <https://doi.org/10.1016/j.nima.2018.04.004>

This is a PDF file of an unedited manuscript that has been accepted for publication. As a service to our customers we are providing this early version of the manuscript. The manuscript will undergo copyediting, typesetting, and review of the resulting proof before it is published in its final form. Please note that during the production process errors may be discovered which could affect the content, and all legal disclaimers that apply to the journal pertain.

# The network of photodetectors and diode lasers of the CMS Link alignment system

P. Arce, J.M. Barcala, E. Calvo, A. Ferrando\*, M.I. Josa, A. Molinero,  
J. Navarrete and J.C. Oller  
*CIEMAT (Madrid, Spain)*

J. Brochero, A. Calderón, M.G. Fernández, G. Gómez, F.J. González-Sánchez,  
C. Martínez-Rivero, F. Matorras, T. Rodrigo, P. Ruiz-Árbol, L. Scodellaro, M. Sobrón,  
I. Vila and A.L. Virto  
*Instituto de Física de Cantabria, CSIC–University of Cantabria (Santander, Spain)*  
J. Fernández  
*University of Oviedo (Oviedo, Spain)*

P. Raics, Zs. Szabó, Z. Trócsnyi, B. Ujvári and Gy. Zilizi  
*University of Debrecen, Institute of Experimental Physics (Debrecen, Hungary)*  
N. Béni, G. Christian, J. Imrek, J. Molnar, D. Novak, J. Pálinkás, G. Székely  
and Z. Szillási  
*Institute of Nuclear Research ATOMKI (Debrecen, Hungary)*

G.L. Bencze and G. Vestergombi  
*KFKI Research Institute for Particle and Nuclear Physics (Budapest, Hungary)*

M. Benettoni, F. Gasparini, F. Montecassiano, M. Rampazzo and M. Zago  
*Dipartimento di Fisica dell'Università di Padova e Sezione dell'INFN (Padova, Italy)*  
A. Benvenuti

*Dipartimento di Fisica dell'Università di Bologna e Sezione dell'INFN (Bologna, Italy)*  
H. Reithler  
*Physikalisches Institut IIIA, RWTH Aachen University (Aachen, Germany)*

C. Jiang

*Institute of High Energy Physics (Beijing, China)*

## Abstract:

The central feature of the CMS Link alignment system is a network of Amorphous Silicon Position Detectors distributed throughout the muon spectrometer that are connected by multiple laser lines. The data collected during the years from 2008 to 2015 is presented confirming an outstanding performance of the photo sensors during more than seven years of operation. Details of the photo sensor readout of the laser signals are presented. The mechanical motions of the CMS detector are monitored using these photosensors and good agreement with distance sensors is obtained.

*Keywords:* CMS, alignment, amorphous silicon photodetectors.

---

\* Corresponding author.

E-mail address: antonio.ferrando@ciemat.es

## 49 1. Introduction

50 A major part of the Compact Muon Solenoid detector (CMS) [1-4] is a powerful  
51 muon spectrometer [3] that identifies and measures muons over a wide range of energy  
52 from a few GeV up to several TeV. The CMS detector basically has a cylindrical  
53 symmetry around the LHC beam pipe, an overall diameter of 15 m, a total length of  
54 21.6 m and weighs 12.5 kt (mainly iron flux return). At its heart, a 13 m long, 6 m inner  
55 diameter superconducting solenoid [2] provides a 3.8 T field along the beam axis and a  
56 bending power of about 12 Tm in the transverse plane. The field return consists of 1.5  
57 m of iron layers interspersed with four muon stations in both the barrel and endcap  
58 regions that ensure full geometrical coverage and sufficient redundancy.

59 The accuracy required in the position measurement of the muon chambers is driven by  
60 the resolution desired in the momentum measurement of high energy muons. CMS is  
61 designed to achieve a combined (Muon System [3] and Tracker [4]) momentum  
62 resolution of 0.5 – 1% for  $p_T \approx 10$  GeV, 1.5 – 5% for  $p_T \approx 100$  GeV and 5 – 20% for

63  $p_T \approx 1$  TeV for the region  $|\eta| < 2.4$ . This momentum resolution requires the knowledge  
64 of the position of the chambers with a precision comparable to their resolution.

65 Simulation studies were performed [5] to quantify the importance of muon chamber  
66 location for the momentum resolution. The solenoidal magnetic field bends charged  
67 particles in  $r\phi$ , the most important coordinate for determining the muon momentum.  
68 Hence, the alignment system should reconstruct the position of the chambers within 150  
69 – 300  $\mu\text{m}$  for MB1 – MB4 and within 75 – 200  $\mu\text{m}$  for ME1 – ME4 (Fig. 1). The tighter  
70 constraints correspond to the first stations (MB1 and ME1) since the magnetic bending  
71 in the return yoke is reversed with respect to the magnetic field in the solenoid and  
72 hence the largest bending and best momentum determination is measured in the first  
73 stations. Since these stations are located immediately outside the magnet before the flux  
74 return they combine with the Tracker hits to achieve the measurement of the muon  
75 momentum.

76 During CMS operations, the movements and deformations of the muon spectrometer  
77 are surely larger than 100  $\mu\text{m}$ . To monitor these motions, CMS is instrumented with an  
78 opto-mechanical alignment system that performs a continuous and precise measurement  
79 of the relative positions of the muon chambers as well as the position of the muon  
80 spectrometer with respect to the tracker, which is aligned independently.

81 In a previous document [6] the alignment system was presented, and, data taken during  
82 the two phases of the 2006 Magnet Test and Cosmic Challenge measured the effects of  
83 the ramp up and down in the magnetic field (magnetic cycle). It was shown that the  
84 Link system produces geometrical reconstructions of relative spatial locations and  
85 angular orientations between the muon chambers and the tracker body with a resolution  
86 better than 150  $\mu\text{m}$  for distances and about 40  $\mu\text{rad}$  for angles.

87 The structural equilibrium of the muon spectrometer was also investigated [7, 8].  
88 Using alignment data from the years 2008 and 2009, it was found that once the  
89 magnetic field intensity reaches 3.8 T, provided that the current in the coils remains  
90 unaltered, the mechanical structures reach equilibrium within the first 24 h. Structural  
91 equilibrium means that any displacement in any direction (axial or radial) remains  
92 within the short distance sensors resolution:  $\pm 40$   $\mu\text{m}$  and any rotation within the tilt  
93 sensors resolution:  $\pm 40$   $\mu\text{rad}$ . These structural equilibrium periods will be referred to as  
94 stability periods.

95 To achieve a precise multipoint position monitoring, one needs to measure and/or  
96 monitor accurately the space position of a laser beam at several points along its path. In

97 such cases the simplest solution is to use transparent position sensors attached to the  
98 pieces whose spatial positions have to be monitored. When the expected independent  
99 motions of the pieces are big (i.e. from mm to a couple of cm) the active area of the  
100 sensors must be large.

101 This paper focuses on the description of the CMS Link alignment network of diode  
102 lasers and photosensors and presents a brief analysis of the corresponding recorded data  
103 during the physics runs in the periods 2008 to 2013 and in 2015. The goal is to show  
104 how the photosensors behave during the magnet cycles and the stability periods, how  
105 compatible these measurements are with previous studies [7] and how their data are  
106 used to help in the CMS geometrical reconstruction.

107 A short description of the CMS Alignment system is given in Section 2. The general  
108 layout, the electronic equivalence and the measurement principle of the amorphous  
109 silicon position detectors (ASPDs), as well as the readout electronics are shown in  
110 Sections 3, 4 and 5, respectively. A summary of the characteristics of the sensors, their  
111 average performance and the tests prior to their installation in CMS are described in  
112 Section 6, while Section 7 deals with the description of the network of photo sensors  
113 and diode lasers of the CMS Link alignment system. The interpretation of the motions  
114 detected by the light spot reconstruction is given in Section 8 and an analysis of those  
115 reconstructions during the magnet cycles and the stability periods is done in Section 9.  
116 Section 10 shows, with a few examples, how the CMS motions detected with the  
117 ASPDs, during the ramping of the magnetic field, correlate with those obtained from the  
118 distance-measuring potentiometers (short distance sensors) used in previous studies [6-  
119 8]. Finally, Section 11 summarizes the results.

120

## 121 **2. The CMS Alignment System**

122 The CMS tracking detectors are grouped into four separate systems: two endcaps, the  
123 central barrel, and the tracker, which is inside the solenoidal coil. Different muon  
124 detection technologies are employed for the central and the endcap regions due to the  
125 different backgrounds and the varying intensity and homogeneity of the magnetic field.  
126 A longitudinal view of one quadrant of the CMS experiment showing the various  
127 detectors is given in Fig. 1.

128 In the barrel region, surrounding the coil of the solenoid, four concentric stations of  
129 drift tube (DT) chambers (named MB1 to MB4), are inserted in the five wheels that  
130 constitute the return iron yoke. A muon chamber is composed of three superlayers. Each  
131 superlayer in turn is made of four layers of drift cells, the basic detection unit. Drift  
132 times are translated into local space positions with a single hit resolution of 250  $\mu\text{m}$ .  
133 Superlayers are arranged to measure the muon in two orthogonal coordinates; two  
134 superlayers measure the muon in the bending plane, and the third superlayer measures it  
135 in the beam axis direction.

136 The mechanical design of a drift chamber is driven by the 100  $\mu\text{m}$  spatial precision  
137 requirement in the determination of the track position in the bending plane. Track  
138 segments are obtained by linear fits to the reconstructed hits in each coordinate. The DT  
139 chambers are subject to variable residual magnetic fields below 0.4 T for all the stations  
140 except for the innermost MB1 chambers closest to the endcaps, where the field reaches  
141 0.8 T.

142 At both CMS endcaps there are four layers of muon chambers, named ME1 to ME4. In  
143 the endcap regions the magnetic field is typically high and very inhomogeneous due to

144 its bending of the flux return. In addition, at the level of the ME1 chambers the field  
 145 intensity may be as high as 3 T. To cope with this and with the high particle fluxes in  
 146 these regions, different gas ionization detectors called Cathode Strip Chambers (CSCs)  
 147 are used. The CSCs are multi-wire proportional chambers in which the cathode plane is  
 148 segmented into strips running across wires, giving 2D information of the particle  
 149 passage. The flux return results in a reversal of the magnetic force on a muon so the best  
 150 measure of the muon momentum occurs in the first station, which has the highest  
 151 resolution requirement (75  $\mu\text{m}$ ). The remaining muon stations require a lower precision  
 152 of 150  $\mu\text{m}$ .

153 Resistive Plate Chambers (RPCs), both in the barrel and in the endcaps, complement  
 154 the muon spectrometer. They are used mainly for trigger purposes since their time  
 155 resolution is better than 2 ns, although their hits may also participate in the muon track  
 156 recognition. The RPCs are assumed to be placed at their nominal positions within their  
 157 spatial resolution of about 1 cm.

158 Typically, the total number of hits including tracker hits registered along a muon track  
 159 is about 40–45 in the forward region and about 55 in the central one ( $|\eta| < 1$ ). The muon  
 160 momentum is measured through the bending of its track in the transverse plane. The  
 161 radius of curvature  $\rho$  and the momentum of the muon in the plane perpendicular to the  
 162 magnetic field ( $p_T$ ) are related by  $\rho[\text{m}] = p_T[\text{GeV}]/0.3 \text{ B}[\text{T}]$ . The radius of curvature is  
 163 obtained from the measurement of the muon trajectory sagitta  $s$ , after traversing a  
 164 distance  $d$  in the magnetic field, using the approximate expression  $\rho = d^2/8s$ . An  
 165 uncertainty in the sagitta measurement results in an uncertainty in the momentum  
 166 measurement.

167 The relative uncertainty in the sagitta measurement is  $\delta s/s = -\delta p_T/p_T$ , proportional to  
 168  $\sigma(s)p_T/d^2B$ , where  $\sigma(s)$  is the resolution in the sagitta measurement. The relative  
 169 uncertainty in the momentum increases with the muon momentum and decreases  
 170 linearly with the magnetic field and quadratically with the traversed distance.

171 A right-handed coordinate system is used in CMS, with the origin at the nominal  
 172 interaction point (IP), the  $x$ -axis pointing to the centre of the LHC ring, the  $y$ -axis  
 173 pointing up (perpendicular to the LHC plane), and the  $z$ -axis along the anticlockwise  
 174 beam direction. The polar angle  $\theta$  is measured from the positive  $z$ -axis and the  
 175 azimuthal angle  $\phi$  is measured in the  $xy$ -plane. The pseudorapidity is a geometrical  
 176 variable defined as  $\eta = -\ln[\tan(\theta/2)]$ .

177 At 3.8 T the solenoid induces an axial force of about 10,000 tons on the endcap iron  
 178 yokes in the direction of the IP. Aluminium blocks, called Z-stops, are located between  
 179 the endcap disks and the barrel region, as well as between the five barrel wheels, to  
 180 prevent the different structures from being crushed into each other. The positions of the  
 181 Z-stops are indicated in Fig. 1. The deformation of the endcap iron disks as a result of  
 182 the compression due to the magnetic forces and the resistance of the barrel Z-stops are  
 183 illustrated in Fig. 2.

184 To meet the momentum resolution requirements the tracker is equipped with an  
 185 internal alignment system and can be treated as a rigid body for purpose of the muon  
 186 alignment system. The CMS Alignment System is therefore organised in three basic  
 187 blocks:

188 – The Tracker alignment system [4] measures the relative position of the various  
 189 tracker modules and monitors eventual internal deformations.

190 – The Muon (Barrel and Endcaps) alignment system [3] monitors the relative  
191 positions among the DT and CSC muon chambers.

192 – The Link alignment system [3] connects the position of the two muon subsystems,  
193 Barrel and Endcaps, to the position of the Tracker and monitors the relative  
194 movements between them.

195 The positions of the Link system sensors define three alignment planes  $60^\circ$  apart,  
196 starting at  $\Phi = 15^\circ$ . Fig. 3 (left) shows one of the  $\Phi$  planes where the three alignment  
197 subsystems can be seen. Each plane contains four independent alignment quadrants  
198 where the three systems are connected.

199 In each  $\Phi$  quadrant six Amorphous Silicon Position Detector sensors (ASPDs) are  
200 connected by laser lines. The full network contains 36 sensors per CMS endcap. An  
201 ASPD sensor [8-10] consists of two groups of 64 silicon micro-strips  $408\ \mu\text{m}$  wide,  
202 with a pitch of  $430\ \mu\text{m}$ , oriented perpendicularly. The total active area is  $\sim 30 \times 30\ \text{mm}^2$ .

203 The measured spatial resolutions of the reconstructed light spot on the sensor active  
204 area are, on average,  $5.2 \pm 2.6\ \mu\text{m}$  and  $5.1 \pm 2.4\ \mu\text{m}$  for the X- and Y-sensor  
205 coordinates, respectively [10].

206 Each of the 12 alignment quadrants use four laser light paths, one originating at the  
207 Tracker, two at the Endcap, and one at the Barrel region as indicated in Fig. 3 (left),  
208 resulting in 48 laser paths, 24 on each side (positive or negative Z) of the detector. Each  
209 laser path, in turn, is monitored by three ASPDs, providing a total of 144 beam spots  
210 over the whole CMS detector.

211 All laser-source collimators are housed in rigid carbon fibre structures called  
212 alignment rings (AR), modules for the alignment of the barrel (MAB), and link disks  
213 (LD) as shown in Fig. 3 (left).

214 The ARs are annular structures attached to the Back Disks (BDs), the outermost,  
215 uninstrumented, Tracker Endcap discs. The LDs, annular structures as well, are  
216 suspended from the inner diameter of the YN1 iron disks of the endcap muon  
217 spectrometer by means of aluminium tubes attached to mechanical assemblies called  
218 Transfer Plates (TPs). MABs are mounted onto the barrel yoke elements.

219 The assumption of “rigid bodies” for the four tracking systems, allows setting up a  
220 redundant system of twelve planes that provide redundancy in case of a malfunctioning  
221 sensor or a missing signal due to large mechanical movements [8]. The  $\Phi$  Link planes  
222 are also depicted in Fig. 3 (right), where the CMS coordinate system is also indicated.

223 The Link System laser-ASPD network is complemented by electrolytic tiltmeters for  
224 angular measurements with respect to the gravity, optical and mechanical proximity  
225 sensors for short distance measurements, aluminium tubes for long distance  
226 measurements, magnetic probes and temperature sensors [6-8]. All sensors are located  
227 inside independent rigid structures, which are individually calibrated and intercalibrated  
228 on special benches and measured later, by photogrammetry [6], after installed in CMS.

229

### 230 3. Amorphous Silicon Position Detecting Sensors

231 The use of semi-transparent photodetectors is very appropriate for the CMS Link  
232 Alignment System due to the fact that optical paths should cross more than one sensor  
233 in the same laser line, as can be inferred from Fig. 3 (left).

234 This is not the unique solution to achieve that purpose, but it is probably the simplest  
235 one and this is why groups at IFCA and CIEMAT, together with Steinbeis-

236 Transferzentrum für Angewandte Photovoltaik und Dünnschichttechnik (STAPD),  
 237 carried out a joint effort to develop a new generation of semi-transparent amorphous  
 238 silicon 2D photosensors (ASPD) for multipoint position detecting purposes. The set of  
 239 ASPD sensors for CMS was manufactured by STAPD with technological support from  
 240 the Universität Stuttgart (Institut für Physikalische Elektronik, IPE) under the quality  
 241 control and acceptance of IFCA-CIEMAT. A complete report on this work can be found  
 242 in Ref. [12].

243 Figure 4 depicts the layer sequence and the general layout of these semi-transparent  
 244 2D sensors. A matrix arrangement of perpendicular ZnO strips enables the precise  
 245 reconstruction of the position of the laser beam, while the a-SiC:H layer sandwiched  
 246 between the ZnO strips provides high optical transmission and photosensitivity at the  
 247 same time. The union of a ZnO strip and the photo conducting a-SiC:H defines a  
 248 Schottky photodiode strip. The position of a light spot onto the sensor surface is then  
 249 reconstructed as the centroid of the local photo responses generated by the 2D matrix of  
 250 photodiode strips.

251 The ASPD sensors incorporate antireflective coated glass substrates delivered by  
 252 Schott Advanced Materials (Grünenplan, Germany). These are special 100 mm diameter  
 253 glass wafers with a high stability against irradiation damage that are selected from a  
 254 production lot for minimum deviation in parallelism of their two surfaces. The  
 255 maximum deviation in thickness was 5  $\mu\text{m}$ . Those high-quality glass wafers receive a  
 256 very homogeneous antireflective coating by Jenoptik (Jena, Germany) which reduces  
 257 reflection losses to less than 0.5 % per surface.

258 By optimizing material properties, deposition, and patterning processes, we achieve a  
 259 layer sequence, which represents an optimum compromise between optical transparency  
 260 and photosensitivity. This optimized ASPD sensor comprises the following layer  
 261 sequence: antireflective coated glass substrate (1 mm), aluminium doped zinc oxide  
 262 ZnO:Al (110 nm), carbon-doped hydrogenated amorphous silicon a-Si<sub>0.9</sub>C<sub>0.1</sub>:H  
 263 (195 nm), and ZnO:Al (110 nm).

264 Top and bottom strips are arranged perpendicular to each other. The width of each  
 265 ZnO:Al strip amounts to 408  $\mu\text{m}$ , with a 22  $\mu\text{m}$  spacing to the neighbouring strips.  
 266 Aluminium bond pads arranged on top of the ZnO:Al strips outside the photosensitive  
 267 area of the sensors provide electric contact to the individual strips by wire bonding to  
 268 the readout electronics board, described later.

269

#### 270 4. ASPD Readout.

271 The photodiodes of the ASPDs are read out in the following way: if  $N_{x(y)}$  is the number  
 272 of photodiodes along the two orthogonal coordinates  $x$  ( $y$ ), they are accessed as a set of  
 273  $N_x + N_y$  rows and columns of photocurrents.

274 Figure 5 illustrates the electronic equivalent circuit for the case of a small 8×8 strips  
 275 sensor with a light spot illuminating 4 strips in each direction. The photocurrents  
 276 generated in each strip diode are extracted through the “ $x_i$ ” and “ $y_i$ ” ends. Measuring the  
 277 photocurrents going through “ $y_1$ ”, “ $y_2$ ”..., “ $y_8$ ” and “ $x_1$ ”, “ $x_2$ ”..., “ $x_8$ ” terminals, the  
 278 projections over the Y and X axis of the light spot intensity are obtained, which are also  
 279 indicated in the figure.

280 In practice, the two coordinates of the light spot centre on the sensor sensitive area are  
 281 determined by double Gaussian fits to the Y and X light distributions, respectively. A  
 282 double Gaussian function is used to account for a possible small amplitude, but large  
 283 width contribution caused by background.

284 Figure 6 (top) and (bottom) show the reconstruction of x and y coordinates of a laser  
285 beam spot incident on the sensor. The curves are the result of fits to the corresponding  
286 photocurrent distributions. The distributions in the insets show the charge collected  
287 from each of the strips (in ADC counts).

288 In this particular example the effective widths of the double Gaussians, calculated as  
289 the amplitude-weighted quadrature sum of the widths of each of them, are 542.0  $\mu\text{m}$  and  
290 537.0  $\mu\text{m}$  in the X and Y coordinates, respectively. The uncertainty in the reconstructed  
291 light spot coordinates in the example is 36.1  $\mu\text{m}$  and 35.8  $\mu\text{m}$  for the X and Y  
292 coordinates, respectively. The uncertainties in the X and Y positions are calculated as  
293 the effective width of the double Gaussian fit divided by the square root of the number  
294 of strips used in the reconstruction (typically 15 if there are no bad strips),

295 The goodness of the Gaussian fits is not uniform over the full sensitive area. Although  
296 the response in terms of mA/W is very homogeneous, the presence of any “bad strips”  
297 in the beam spot area diminishes the degrees of freedom in the Gaussians fits to the  
298 current distributions. A strip is called “bad” if it does not provide any electrical signal  
299 usable for the light spot centre reconstruction.

300 Electrical defects that may occur during ASPD processing can be classified into two  
301 main types. First, an in-plane connection between two neighbouring strips causes the  
302 photocurrent signals of both neighbouring strips to approximately double under uniform  
303 illumination. The second major type of defect is a short circuit through the layer stack in  
304 the vertical direction. Particles from the environment or from a deposition tool are  
305 electrostatically captured at the glass substrate. Such adsorbed particles may be released  
306 at any stage of the processing sequence forming a pinhole. Depending on the specific  
307 processing step, the resulting defect introduces a vertical electric contact between the  
308 top and bottom ZnO:Al strips. As a consequence, the affected row(s) and column(s) of  
309 the sensor will exhibit an electrical response independent of the illumination.

310

## 311 **5. Readout electronics**

312 Custom electronics for the readout of the sensor photocurrents and the subsequent  
313 Gaussian fits has been designed and constructed at CIEMAT. The electronics consists  
314 of a sensor carrier, holding the sensor, coupled to the front-end (FE) electronics (two  
315 signal multiplexer boards) and a signal processor or Local Electronic Board (LEB).

316

### 317 ***5.1 The sensor carrier and the signal multiplexer boards***

318 The ASPD sensor is mounted on the carrier board with two perpendicular pads  
319 containing 64 gold-terminated pads for reading out the signals of the sensor. Two  
320 64-pin miniature connectors link the photocurrents from the ASPD sensor to the  
321 multiplexer boards.

322 The multiplexer boards (named “horizontal” and “vertical”) are each mounted  
323 perpendicular to the carrier board as shown in Fig. 7 (left). These multiplexer boards  
324 accept currents from the ASPD sensor as well as control signals from the LEB.

325 Eight multiplexers (16:1), for photocurrent switching, are mounted on the boards. Four  
326 multiplexers (64 channels) are used for the top electrodes (y-axis vertical multiplexers)  
327 and the other four (64 channels) for the bottom electrodes (x-axis horizontal  
328 multiplexers).

329 To bias the Schottky photodiodes, which are the active elements of the ASPD, each  
330 top electrode of the sensor is connected to analog ground (AGND) through a 47 k $\Omega$   
331 resistor and each bottom electrode, in turn, is connected to the analog bias voltage  
332 (ABIAS) through a similar 47 k $\Omega$  resistor. Each strip of the bottom and top electrodes is  
333 connected to a multiplexer input.

334 The sensor carrier and the multiplexer boards are mounted in an open-cube set-up,  
 335 with only three faces as shown in Fig. 7 (right), of 4.7 cm per side. This arrangement is  
 336 a technical solution that minimizes the dimensions of the complete detector unit to  
 337  $4.7 \times 4.7 \text{ cm}^2$  in the plane perpendicular to the light path.

### 338 339 **5.2 Local Electronic Board (LEB)**

340 The Local Electronic Board is the signal processor board that controls the ASPD  
 341 readout. It converts current to voltage, digitises analog signals, reconstructs the light  
 342 beam spatial position coordinates and communicates with a central PC. A single LEB  
 343 can control up to 4 ASPD sensors simultaneously.

344 The LEB board block diagram is shown in Fig. 8 a). In the Link alignment system, the  
 345 LEBs communicate with each other through a specific bus, the *Bus Interface (BI)*. The  
 346 LEBs incorporate a CAN Interface card (CI), which consists of a CAN driver (DRV), an  
 347 opto-coupled interface (OI) and a CAN controller (CC), that allows the LEBs to  
 348 communicate with other LEBs and with a central PC via the CANbus communication  
 349 protocol.

350 An *ASPD Control Interface (ACI)* generates and sends control signals to up to 4  
 351 remote ASPD sensors. The *ASPD Signal Conditioner (ASC)* converts output currents to  
 352 voltage and adapts the voltage levels to the ADC input voltage range. The current to  
 353 voltage conversion proceeds in two steps. First, a high precision resistor is used as  
 354 feedback of an operational amplifier in order to convert current to voltage. In the second  
 355 step a variable-gain amplifier adapts the signal to the ADC input range. Gains are  
 356 adjustable and may be different for each sensor in a chain and even different for  
 357 horizontal and vertical strips in a given sensor. In this way, at the beginning of a CMS  
 358 data run gains, and laser output power are adjusted as needed.

359 To overcome eventual environmental radiation effects (including latchup), fault  
 360 tolerant mechanisms are implemented by a *Redundant Controller System* with a *Fault*  
 361 *Tolerant Interface (FTI)*, which controls the LEB operation in a redundant mode. It  
 362 includes two *Micro Controller Units (MCU, Hitachi, H8S/2357)* and the interface  
 363 between them.

364 A *Fault Injection board interface (FI)* is used to program the MCUs via an RS-232  
 365 serial port. It controls fault injection procedures and communicates with an external  
 366 application.

367 Finally, a *Programming Interface (PI)* allows one to configure the MCUs  
 368 programming. It supports two programming modes: via PC and cloning through the FI  
 369 board.

370 The photograph in Fig. 8 b) shows an uncovered LEB after mounting all of its  
 371 components.

### 372 373 **6. Sensor performance and testing.**

374 A total of 122 ASPD units were constructed following the processes explained in Ref.  
 375 [12]. An experimental procedure was developed in order to fully characterize the  
 376 performance of each of the sensors prior to installation in the CMS detector. Results of  
 377 this characterization are reported in Ref. [13]. From the total sample 72 sensors were  
 378 installed in the detector, 36 per CMS Z side; 50 were left as spares.

379 In Table 1 the average performance of the 122 sensors show a photosensitivity of  
 380  $16.3 \pm 7.6 \text{ mA/W}$  and a spatial point resolution of  $\sigma_x = 5.2 \pm 2.6 \text{ }\mu\text{m}$  and  $\sigma_y = 5.1 \pm 2.4$   
 381  $\mu\text{m}$ . For a beam of light at perpendicular incidence to the given sensor face, the  
 382 deflection angles where  $\Theta_x = -1.1 \pm 5.8 \text{ }\mu\text{rad}$  and  $\Theta_y = 0.8 \pm 3.8 \text{ }\mu\text{rad}$ , where  $\Theta_x$  and  $\Theta_y$

383 are the components along the x- and y-axis. The measured average transmittance T is  
384  $84.8 \pm 2.9 \%$ . The most important construction parameters of the ASPD sensors, already  
385 discussed in Sections 3 and 4, are summarized in Table 2.

386 Those ASPD sensors and their associated electronics are designed to remain operative  
387 under the hostile environmental conditions of CMS such as high magnetic fields or high  
388 levels of irradiation. A clear confirmation of the robustness of the sensors is the  
389 observation that after more than seven years of operation in the CMS detector not a  
390 single ASPD sensor needed replacement.

391 The operation of the ASPD sensors is unaffected by the large magnetic field, since the  
392 short carrier-drift distance and the low Hall mobility of the amorphous silicon [12] has a  
393 small effect on the position resolution (i.e. less than  $1 \mu\text{m}$  at 4 T).

394 Irradiation tests, for the sensors and their FE electronics were performed with gamma  
395 rays at the NAYADE [14] facility at CIEMAT and with thermal neutrons at the MGC-  
396 20 Cyclotron of ATOMKI [15], in Debrecen. The results [16] proved that the a-Si  
397 material could withstand an irradiation up to 100 kGy photons (at a rate of 3kGy/h) and  
398 up to  $10^{15} \pm 37\%$  neutrons/cm<sup>2</sup> fluence without any degradation in the sensor  
399 performance.

400 The resistors and capacitors in the front-end electronics also remain operational after  
401 receiving these doses. Multiplexers (DG406, 16:1, from SILICONIX) are expected to  
402 be less radiation-hard than all other components, but, none of them have failed so far.

403 The most delicate component inside the LEB is expected to be the Microcontroller  
404 Unit so the behaviour of the Hitachi H8S/2357 MCU under photon and proton beams  
405 was investigated. Nine MCU devices were irradiated, in real operation conditions, with  
406 gamma-rays from a <sup>137</sup>Cs source at the IR14 facility of CIEMAT and with 60 MeV  
407 protons at the CYCLONE [15] installation of the Université Catholique de Louvaine  
408 (Belgium). The photon irradiation reached 210 Gy, and the total proton fluence was  $1.5$   
409  $\times 10^{11} \text{ cm}^{-2}$ .

410 The results [17] were very satisfactory: no malfunctions were detected due to the  
411 irradiation dose; during proton tests, only a few bit upsets in the SRAM memory  
412 occurred. No Single Event Latch-ups (SELs) were produced, and no Flash Memory or  
413 Single Event Effects (SEEs) were detected.

414 The most radiation-hard element of the configuration is the ASPD sensor. The  
415 associated LEB electronics, which is much less radiation tolerant, is located in the  
416 balconies of the CMS experimental area. The signal is carried from the ASPDs to the  
417 LEB ADC converter through more than 20 m long twisted pair cables.

418

## 419 **7. Layout of photo sensors and diode lasers of the Link alignment system**

420 A sketch of one quadrant of a  $\Phi$  Link alignment plane with its instrumentation is  
421 shown in Fig. 9. In each  $\Phi$  quadrant six Amorphous Silicon Position Detector sensors  
422 (ASPDs) are connected by laser lines, as detailed in Fig. 10.

423 The four light paths of the network originate at the three collimators installed in each  
424 of the  $\Phi$  quadrants, as sketched in Fig. 10. As an example, Light Path L2 starts at the  
425 collimator located in the Laser Box. The Laser Box (LB), attached to the Link Disk  
426 (LD), is a small optical bench (see sketches in Fig. 11) containing the LD collimator, a  
427 modified rhomboidal prism that splits the laser beam into two parallel beams about 5  
428 cm apart, and a semi-transparent mirror that allows the LD laser light to pass through  
429 and reflects the laser beam (Light Path L3) coming from the AR.

430 The data taking procedure for each quadrant (see Figs. 10 and 11) is as follows. First,  
431 the AR laser turns on and the beam outgoing from the corresponding collimator (Light

432 Path L3) arrives to the Laser Box mirror and is deflected to the sensors P1 (placed on  
 433 the Transfer Plate), P2 and P3 (both located in the MAB). Distances are:  $d(\text{AR-LB}) =$   
 434  $3.682$  m,  $d(\text{LB-P1}) = 2.151$  m,  $d(\text{P1-P2}) = 1.654$  m, and  $d(\text{P2-P3}) = 2.538$  m. The total  
 435 L3 Light Path length is then  $10.025$  m.

436 Then, the AR laser is switched off and the external MAB laser is turned on. The  
 437 corresponding collimator, installed in the Laser Level (LL) attached to the MAB (see  
 438 sketches in Fig. 12), sends a beam (Light Path L1) that crosses in sequence the sensors  
 439 P3, P2 and P1. The distance between the collimator on the MAB and sensor P3 is  
 440  $0.010$  m.

441 Finally, the Laser Level (MAB Laser in Fig. 10) is switched off and the LD laser  
 442 (whose collimator is installed in the LB) is turned on. The collimator in the Laser Box  
 443 sends a beam that is split into two by the modified rhomboidal prism. One of the beams  
 444 (Light Path L2) crosses the sensors P1, P2 and P3, while the second one (Light Path L4,  
 445 parallel to the first one) crosses sensors P4 (at the TP), P5 and P6 (both attached to the  
 446 ME/1/2 chamber). The distances are  $d(\text{P4-P5}) = 0.067$  m and  $d(\text{P5-P6}) = 1.736$  m.

447 The full sequence of lasers turning on and off, reading out of photocurrents in the  
 448 sensors and reconstruction of the centres of the light spots on the ASPD surfaces  
 449 constitutes a full data cycle set and takes slightly more than half an hour to complete.  
 450

### 451 **7.1 Light spot resolutions**

452 The laser beam in a given light path crosses a first sensor and then reaches a second  
 453 with an incidence angle (in the X and the Y directions) that follows a Gaussian  
 454 distribution with central value and width (rms) as measured in the characterization  
 455 process of the first sensor. The reconstruction uncertainty in the second sensor,  $\sigma_2(\text{rec})$ ,  
 456 is therefore affected by an additional term, related to the uncertainty in the deflection  
 457 angles, that can be written as:  $\sigma_2^{\text{def}} = \sigma_1(\text{def}) \times d_{12}$  (where  $\sigma_1(\text{def})$  is the width of the  
 458 deflection angle distribution of sensor 1 and  $d_{12}$  the distance between sensors 1 and 2),  
 459 to be added quadratically to the spatial reconstruction resolution of the second sensor.

460 The light ray is subsequently deflected in each of the downstream sensors in the given  
 461 light path, always according to their measured values of deflection angles. In general,  
 462 the resulting incidence angular distribution on the sensors surfaces is the convolution of  
 463 the deflections happening successively in the upstream sensors, each of them having its  
 464 own Gaussian-like distribution. The average deflection in sensor “j”, due to the presence  
 465 of several upstream sensors “i” ( $i = 1, j-1$ ), can therefore be written as:

$$466 \Delta_j = \sum_{i=1, j-1} (\Theta_i \times d_{ij}) \quad (1)$$

467 where  $\Theta_i$  is the deflection angle of sensor “i”. The uncertainty induced in the  
 470 reconstruction process in sensor “j” can be expressed as:

$$471 \sigma_j = \{ \sigma_j^2(\text{rec}) + \sum_{i=1, j-1} [\sigma_i(\text{def}) \times d_{ij}]^2 \}^{1/2} \quad (2)$$

473

474 The above expressions apply to both coordinates, X and Y.

475 The value of  $\sigma_j$  is precisely the resolution in the detection of displacements of the  $j^{\text{th}}$   
 476 sensor in the line: the quantity that will determine whether a given sensor has moved or  
 477 not from its initial position in the beam light. This quantity defines the spatial point  
 478 reconstruction resolution of a given sensor inside its light path and will be used as the  
 479 uncertainty in the light spot coordinates reconstruction. For the CMS network  $j_{\text{max}} = 3$ .

480 The data recorded by the Optical System Network in the quadrant  $\Phi = 75^\circ$  at the +Z  
 481 side has been arbitrarily chosen to study the response of the ASPDs in operation for the  
 482 years 2008 through 2013 and in 2015. A priori, there should be no difference in the  
 483 behavior of the different quadrants.

484

## 485 **7.2 Characteristics of the sensors placed at the $\Phi = +75^\circ$ quadrant**

486 The six ASPDs placed in the  $\Phi = 75^\circ$  quadrant at the +Z CMS side have the  
 487 characteristics [13] shown in Tables 3 and 4.

488 For ideal conditions Table 5 shows the calculated resolutions in the reconstruction of  
 489 the various light spots for that quadrant, using the measured characteristics of the ASPD  
 490 sensors, P1 to P6, crossed by the corresponding L1 to L4 laser lines [12]. All quantities  
 491 appearing in Table 5 are given in micrometres.

492 The quoted uncertainties are calculated using the eq. (2), the measured sensor  
 493 characteristics in Tables 3 and 4 and the appropriate sensor to sensor distances, *in ideal*  
 494 *conditions*. This means that they represent the expected uncertainties in the absence of  
 495 any major distortion of the laser light due to air density changes and assuming that the  
 496 beam light arrives in a direction approximately normal to the sensitive face and, of  
 497 course, no mechanical motion of the rigid mechanical structures where they are  
 498 attached. These requirements are rarely fulfilled by the laser light paths.

499 As mentioned, the distribution of photocurrents in the vertical (horizontal) strips are  
 500 used to reconstruct the sensor local X (Y) coordinate of the light spot (see Figs. 6 and  
 501 7). The light spot reconstruction in the sensors is referred to their geometrical center,  
 502 whose coordinates are taken to be (0, 0). Since the strip pitch is 0.430 mm and the spot  
 503 cannot be reconstructed beyond the centers of strips 0 and 63, the effective sensor limits  
 504 are  $\pm 13.545$  mm in both directions and the usable active area of an ASPD is then  $\sim 27 \times$   
 505  $27 \text{ mm}^2$ .

506 The sensor coordinate system is sketched in Fig. 13: X- and Y-axis are the detector  
 507 local coordinates. The beam in the figure is drawn incoming towards the active face of  
 508 the sensor. In the Link System operation this is not always the case: there are sensors  
 509 receiving the laser beam from the glass face side. Moreover, some of them receive laser  
 510 light from both sides (although never simultaneously). The reception of light for one or  
 511 the other sensor sides affects mainly the deflection angles, but not the light  
 512 transmission, nor the light spot reconstruction. On the other hand, sensors on their  
 513 supporting plates are attached to different CMS elements in different orientations, as  
 514 can be inferred by looking at Figs. 9 and 10.

515 In fact, when the light spot reconstruction data are used in the COCOA reconstruction  
 516 software [18] to determine the position of the photodetectors of the alignment network,  
 517 the knowledge of the real space position of the physical ASPDs derived from the  
 518 reconstruction of the light spots, is dominated by the uncertainty in their absolute spatial  
 519 positions given by photogrammetry [6], about 300  $\mu\text{m}$  for positions and 100  $\mu\text{rad}$  for  
 520 orientations.

521 COCOA (CMS Object oriented Code for Optical Alignment), is an object oriented  
 522 C++ software that handles the data provided by the CMS Alignment system and allows  
 523 the reconstruction, at any moment, of the CMS geometry. For the Muon alignment  
 524 system, COCOA might work with about 3000 parameters for the Link system, which  
 525 are the possible positions and orientations of all the pieces that build up the system  
 526 (distancemeters, collimators, prisms, ASPDs, tiltmeters, structures containing these  
 527 systems, etc.). These parameters serve to actually constraint around 250 free parameters  
 528 (declared as “unknown” or “calibrated” within certain error) inside the fitting code.

529

### 530 **8. Light spots reconstruction and interpretation of motions**

531 In what follows we will analyze some aspects of the data recorded by the ASPDs Link  
 532 System Network, during the first seven years of CMS operation, for the indicated  $\Phi =$   
 533  $75^\circ$  quadrant of the +Z CMS side.

534 In the positive CMS Z side (or +Z side), photo sensors in the MABs are installed in  
 535 such a way that a motion of the reconstructed light spot along the sensor +X local axis  
 536 corresponds to a displacement along the  $+r\phi$  CMS coordinate of the physical sensor (the  
 537 ASPD itself), and a motion of the reconstructed light spot along the sensor +Y local axis  
 538 corresponds to a displacement of the ASPD along the  $-Z$  CMS coordinate.

539 For the ME1/2 sensors, a motion of the reconstructed light spot along the local +X  
 540 (+Y) axis of the sensor corresponds to a displacement along the  $-r\phi$  (+Z) CMS  
 541 coordinate of the physical sensor.

542 For the ME1/1 Transfer plate sensors, a motion of the reconstructed light spot along  
 543 the local +X (+Y) axis of the sensor corresponds to a displacement along the  
 544  $+r\phi$  (+Z) CMS coordinate of the physical sensor.

545 In the negative CMS Z side (or  $-Z$  side), for the MAB sensors, a motion of the  
 546 reconstructed light spot along the local +X (+Y) axis of the sensor corresponds to a  
 547 displacement along the  $+Z$  ( $+r\phi$ ) CMS coordinate of the physical sensor.

548 For the ME1/2 sensors, a motion of the reconstructed light spot along the local +X  
 549 (+Y) axis of the sensor corresponds to a displacement along the  $-Z$  ( $-r\phi$ ) CMS  
 550 coordinate of the physical sensor.

551 For the ME1/1 Transfer plate sensors, a motion of the reconstructed light spot along  
 552 the local +X (+Y) axis of the sensor corresponds to a displacement in the  $-Z$  ( $+r\phi$ ) CMS  
 553 coordinate of the physical sensor.

554 Given that in principle the laser beam path is fixed, when looking at the Laser Path L1  
 555 at the  $+75^\circ \Phi$  quadrant (see Fig.10), a variation in the reconstructed +X local coordinate  
 556 of the light spot on the sensor P2 (or P3) would correspond to a rotation in the  $+\Phi$  CMS  
 557 coordinate of the given sensor while a variation in the reconstructed +Y local coordinate  
 558 of the light spot on the sensor corresponds to a displacement in the  $-Z$  CMS coordinate  
 559 of the sensor.

560 In the same way, a variation in the reconstructed +X local coordinate of the light spot  
 561 on the sensor P1 would correspond to a rotation in the  $+\Phi$  CMS coordinate of the given  
 562 sensor while a variation in the reconstructed +Y local coordinate of the light spot on the  
 563 sensor corresponds to a displacement in the  $+Z$  CMS coordinate of the sensor.

564 Therefore, for two reconstructions of the light spot done at different times, 1 and 2, the  
 565 interpretation in terms of the CMS variables, at the +Z CMS side, for the sensors P2 and  
 566 P3 are:

$$567 \quad \arctg((X_2^{\text{spot}} - X_1^{\text{spot}})/RPI) = \Delta\Phi_{\text{sensor}} \quad (\text{with } I = 2,3)$$

568 where the R positions of the ASPDs are  $RP2 = 4.423$  m and  $RP3 = 6.961$  m

569 and

$$570 \quad -(Y_2^{\text{spot}} - Y_1^{\text{spot}}) = \Delta Z_{\text{sensor}}$$

571 While for sensor P1:

$$572 \quad \arctg((X_2^{\text{spot}} - X_1^{\text{spot}})/RP1) = \Delta\Phi_{\text{sensor}}, \text{ with } RP1 = 2.151 \text{ m}$$

573 and

$$574 \quad Y_2^{\text{spot}} - Y_1^{\text{spot}} = \Delta Z_{\text{sensor}}$$

575 The interpretation of the results is not unique, since the measured relative  
 576 displacements and/or rotations of sensors P1, P2 and P3 may be, as pointed out above, a  
 577 consequence of the convolution of displacements and/or rotations of the following  
 578 elements: MAB, TP, LD and AR. The complete interpretation can only be made by a  
 579 full geometrical reconstruction of the whole set of Link data in a given event by the  
 580 COCOA software.

581 Not all laser spots are correctly reconstructed. Sometimes, one or more lasers might  
 582 miss their target, resulting in wide spots consistent with pure background. Other times,  
 583 the sensors themselves can have several strips damaged by dirt or occasional strip  
 584 readout failure. Clearly, badly reconstructed laser positions can severely bias the final  
 585 geometry reconstruction, and therefore, for the laser spots the errors in the X and the Y  
 586 positions are required to be smaller than  $500 \mu\text{m}$ . This guarantees, in principle, a good  
 587 light spot reconstruction. Only well-reconstructed spots are fed to COCOA.

588 Given that the laser beams travel long distances, go through polarizers, collimators and  
 589 optical fiber junctions, some reconstructed spots might actually become quite wide, and  
 590 a visual inspection of all reconstructed light spots is necessary to make sure we do not  
 591 reject spots which might not pass the criteria due to an unusually large width but which  
 592 otherwise look reasonable.

593 In the following subsections, the reconstructed light spot coordinates on the various  
 594 ASPDs originated by the four laser lines at the indicated  $\Phi$  quadrant is studied over the  
 595 seven years of operation. For simplicity, the discussion, when dealing with motions,  
 596 will be restricted to the displacements along  $\Delta Y_{\text{sensor}}$ , since the relative movements  
 597 along this local coordinate always correspond to the same global CMS direction and are  
 598 easier to interpret without the need of a full reconstruction.

599

## 600 **9. The behaviour of the ASPD data during CMS running**

601 In Ref. [8], the general CMS mechanical motions during the Magnet Cycles and the  
 602 structural equilibrium during the Stability Periods were investigated. A *Magnet Cycle* is  
 603 defined as the operating time between the switching on and off of the current in the  
 604 coils. During the ramping up of the current, from 0 to about 19 kA, the induced  
 605 magnetic field in the solenoid goes from 0 to about 3.8 T. The enormous axial magnetic  
 606 force pushing both CMS endcaps towards the geometrical centre of the detector induces  
 607 important mechanical deformations/motions.

608 The structural equilibrium is achieved 24 h after the working magnetic field (3.8 T) is  
 609 reached [7]. Structural equilibrium is defined as a period during which displacements in  
 610 any direction (axial or radial) remain within the distance sensors resolution of  $\sim 40 \mu\text{m}$   
 611 and any rotation will be smaller than the tilt sensors resolution of  $\sim 40 \mu\text{rad}$ . Periods  
 612 satisfying these constraints are called *Stability Periods* (SPs).

613 From the analyzed data in Ref. [8] the present document will use the ASPDs records  
 614 corresponding to the SPs presented in Table 6 and, when available, the data taken at  
 615  $B = 0 \text{ T}$  immediately before and after the observed SP will also be used.

616 The columns in Table 6 are the year, the Magnet Cycle containing the SP inspected,  
 617 the Stability Period when the data are taken, the working magnetic field intensity, the  
 618 switch off conditions and the number of ASPDs recorded events in that SP,  
 619 respectively. The first data analyzed during a SP is the one taken 24 hours after the  
 620 working magnetic field intensity is reached. In one day a maximum of two full ASPD  
 621 data events (72 photo sensors, 144 light spots reconstructed coordinates) are recorded.  
 622 There are days where no data are recorded.

623 In what follows the data taken from the photo sensors network, both during stability  
 624 periods or magnet cycles, is studied and discussed.

625

## 626 **9.1 Stability Periods**

627 To inspect possible motions of the photosensors during Stability Periods the following  
 628 two items are investigated: the spatial distribution of the reconstructed light spots on the  
 629 sensors surface (no distinction between active or glass sides) and the results from a  
 630 clustering analysis of the impact points.

631

### 632 **9.1.1 ASPD data during the Stability Periods**

633 Figures 14 to 20 show the reconstructed light spots during the Stability Periods (see  
 634 Table 6) in the years 2008 to 2015, respectively.

635 Each row in the figures corresponds to one of the four Light paths, L1 to L4, shown in  
 636 Fig. 10. L1 crosses in sequence sensors P3, P2 and P1 (plots in columns 1 to 3 on the  
 637 first row, respectively). Light paths L2 and L3 do the same through P1, P2 and P3 (plots  
 638 in columns 1 to 3 on the second and the third rows, respectively). Light path L4 crosses  
 639 ASPDs P4, P5 and P6 (plots in columns 1 to 3 on the last row, respectively). In each of  
 640 the three drawings in a given row the beam spots are represented by their X and Y, local  
 641 to the corresponding sensor, reconstructed coordinates.

642 To use the same scale for all twelve plots and for all years, we choose a large range  
 643 which covers most of the sensor area, and, as a result, very often the dots are printed on  
 644 top of each other. The number of entry pairs of (X, Y) spot coordinates are 23, 15, 44,  
 645 46, 187, 64 and 30 for the years 2008 to 2015, respectively, as shown in Table 6.

646 From the observation of these figures, the reader may suspect that certain degradation  
 647 can be observed as time goes by. For example, the distribution of reconstructed light  
 648 spots on sensor P3 in the line L3 from the year 2010 and onwards looks almost random.  
 649 However, the response of the same sensor in the line L2 does not show any suspicious  
 650 behavior. The most probable explanation is that after the CMS closing before the 2010  
 651 physics run, the collimator sitting at the AR in the quadrant  $\Phi = +75^\circ$  became slightly  
 652 mechanically unstable, allowing small oscillations, most probably due to air currents  
 653 originated by temperature changes near the Tracker endcaps. It is important to notice  
 654 that the Tracker was installed in CMS prior to the 2010 physics run.

655 Since L3 is the longest and most complex light path of the system, small collimator  
 656 oscillations could easily cause the laser beam to miss the target sensor. If this happens,  
 657 the readout would only register background illumination and, as a result, the Gaussian  
 658 fit to reconstruct the light spot center becomes very unstable, causing the reconstructed  
 659 beam spot positions to look essentially random.

660 The consequences of the oscillations are more evident in sensor P3 because is the most  
 661 far from the L3 collimator, the last to be crossed in this light path. It happens that  
 662 sometimes the fake coordinate is only the X as in Fig. 17, the Y as in Fig. 20, or in both  
 663 of them (Figs. 18 and 19). In all of these cases a visual inspection of the light spot  
 664 reconstruction is needed, as already said, before feeding any pair of coordinates to  
 665 COCOA.

666 The peculiar light spot reconstructions on sensor P4 at the light path L4 in the last two  
 667 years (2013 and 2015), showing points somehow parallel to the Y coordinate, may be  
 668 caused by dust affecting some horizontal strips, resulting in a non-unique reconstruction  
 669 of the Gaussian-like distributions, or spurious light reflections misidentified as  
 670 originated by a laser beam.

671 None of these suspicious light spot reconstructions are used in the CMS geometrical  
 672 reconstruction software, but, since there are 12  $\Phi$  sectors, the full data results are, as  
 673 already pointed out, sufficiently redundant.

674

### 675 *9.1.2 Clustering of light spots*

676 From the reconstructed coordinates of the light spots displayed in Figs. 14 to 20, the  
 677 distances on the active surfaces of the corresponding ASPD sensors between the first  
 678 reconstructed spot and all the others in a given Stability Period were calculated.

679 The distance between the first reconstructed spot  $(x_o, y_o)$  and that of number  $i$  is given  
 680 by

$$681 \quad d_i = \sqrt{[(x_i - x_o)^2 + (y_i - y_o)^2]},$$

682 where the pair  $(x_i, y_i)$  denotes the reconstructed coordinates of a light spot, as shown in  
 683 Fig. 21. The distribution of the distances  $d$  in each of the sensors, for each of the light  
 684 paths during a given year, was investigated.

685 The quantities obtained from the distributions are the mean value of  $d$ , which is useless  
 686 since it depends on the arbitrary reference  $(x_o, y_o)$  used, and the RMS of the distribution  
 687 of the  $d_i$  values. The RMS is the quantity that shows how close the reconstructed light  
 688 spots are from each other and therefore, quantifies the stability of the laser beams over  
 689 the observed year. A large RMS value may even be due to the existence of various  $d$   
 690 distributions because of changes in the laser beam direction for different reasons  
 691 (among them: sensor or collimator displacement, CMS deformations, etc.).

692 The results are displayed in Tables 7 to 10. The set of reconstructed light spot  
 693 coordinates can be considered stable if the RMS of the corresponding distribution of  
 694 distances is smaller than the general 300  $\mu\text{m}$  uncertainty. In all, Tables 7 to 10 shows  
 695 what was discussed from Figs. 14 to 20; in most cases the numbers show a good  
 696 stability in the reconstructed coordinates of the light spots for a given sensor in a given  
 697 Light path. Discrepancies have understandable explanations and are not due to sensor  
 698 malfunctions.

699

## 700 **9.2 Magnet Cycles**

701 From the laser light spot reconstructions of the X and Y coordinates during the  
 702 Magnet Cycles cited in Table 6, the following quantities were calculated: 1) the  
 703 repositioning, or difference between the X and Y reconstructed coordinates at  $B = 0$  T  
 704 before and after the Stability Period in each of the sensors; and 2) the amplitude of the  
 705 motion, or difference between the X and Y reconstructed coordinates at  $B = 0$  T and  $B$   
 706  $= 3.8$  T due to the motions induced in the mechanical structures supporting  
 707 photodetectors and laser collimators when the magnetic field increases from zero to the  
 708 working intensity.

709

### 710 **9.2.1 Repositioning**

711 The repositioning, or difference between the X and Y reconstructed coordinates  
 712 (denoted by  $\Delta X_r$  and  $\Delta Y_r$ , respectively) at  $B = 0$  T, before and after a given Stability  
 713 Period, in each of the sensors, are given in Tables 11 to 14. Each table corresponds to  
 714 one of the four Light Paths and their associated sensors.

715 Distances are given in microns. Quantities smaller than the assumed  $300 \mu\text{m}$  spatial  
 716 position uncertainty, denote a good reproducibility of the place occupied before the  
 717 ramping up and down of the magnetic field intensity. When larger than this value, the  
 718 quantity is printed in bold. Differences marked \*\*\*\* mean that at least one pair of point  
 719 coordinates at  $B = 0$  T was missing, either because of a non-accepted reconstruction or  
 720 because the laser beam missed the sensor.

721 In spite of the fact that some of the  $B = 0$  T conditions from 2010 onwards were  
 722 uncontrolled, the light spots after the magnet cycle are reconstructed at a distance  
 723 smaller than  $300 \mu\text{m}$  from the light spot previous to the ramping up of current in the  
 724 coils in about 90% of the cases. On the other hand, the instability problem of the AR  
 725 collimator from 2010 onwards becomes very visible in Table 13.

726

### 727 **9.2.2 Largest displacements**

728 The largest displacement corresponds to the difference in the X and Y reconstructed  
 729 coordinates between  $B = 0$  T and  $B = 3.8$  T due to the motions induced by the magnetic  
 730 forces.  $\Delta X_d$  and  $\Delta Y_d$ , are displayed in Tables 15 to 17 for the sensors in the Light Paths  
 731 L1, L2 and L4, respectively. Light Path L3 does not provide reliable measurements due  
 732 to the already cited AR collimator instability.

733 Notice that in Tables 15 to 17 the differences are given in millimeters. Uncertainties,  
 734 which are not quoted, are assumed to be  $300 \mu\text{m}$ , taken as the general reconstruction  
 735 uncertainty.

736 Since the light paths are quite different from each other in length, environmental  
 737 conditions (in particular the air density), collimators pointing with orientations far from  
 738 that of perpendicular incidence, etc., the detected motions (or absence thereof) are not  
 739 identically reproduced by the three investigated lines.

740 In addition, the quality of the response of the ASPDs themselves may change from  
 741 beam path to beam path, due, in particular, to the nonuniform response over the full  
 742 photo-sensitive area, most of the time related to the location of the nonworking strips  
 743 with respect to the laser beam impact point.

744 The Light Paths are sketched in Fig. 10. The *largest displacement* results displayed in  
 745 Tables 15 to 17 are, mostly, a consequence of the deformation sketched in Fig. 2. The  
 746 displacement  $\Delta Y_d$  observed in the location of P1 (Table 12) corresponds essentially to  
 747 the displacements in Z of about 10 mm towards the Interaction Point of both the Laser  
 748 Box at the Link Disk, where the collimator is placed, and of the Transfer Plate (TP, see  
 749 Figs. 9 and 22), where P1 (right sensor in Fig. 22) and P4 (left sensor in Fig. 22) are  
 750 installed [7]. The TP is on top of the Radial Profile (RP) and attached to the YN2 iron  
 751 yoke as shown in Fig. 9.

752 Similarly, the  $\Delta Z$  displacement of the LD, where the Laser Box is installed, due to the  
 753 deformation in Fig. 2, finds a  $\Delta Y_d \approx -10$  mm motion in the reconstruction of the laser  
 754 light spot on the sensor P2 (Table 16). An FEA analysis performed in 1997 before the  
 755 iron disks were constructed shows that in the vicinity of the laser lines the deflection is  
 756 expected to be  $\approx 11$  mm [2]. On the other hand, the external MABs cannot shift very  
 757 much towards each other (just a couple of millimeters) because the barrel iron disks are  
 758 compressed by the z-stops and only move a small amount.

759 Finally, the  $\Delta Y_d \approx 3$  (7) mm motion of the reconstructed light spot over the P5 (P6)  
 760 surface (Table 17) in the light path L4 (collimator inside the LB of the LD) is a result of  
 761 the convolution of two movements: the LB moves towards the IP by an amount of the  
 762 order of 10 mm, and the ME/1/2 chamber also moves in this direction by a smaller  
 763 amount, and also tilts in such a way that P6 stays behind in Z with respect to P5 (also a  
 764 consequence of the deformation sketched in Fig. 2). All motions are therefore  
 765 understood and within the expectations.

766

## 767 10. Correlation of motions

768 In Section 9 we interpreted the  $\approx -10$  mm  $\Delta Y_d$  largest displacement of the sensor P1  
 769 (Laser Path L1, Table 15) in terms of the expected deformation of the endcaps due to  
 770 the magnetic field forces which cause displacements of both the collimator installed in  
 771 the Laser Box (LB) located at the Link Disk (LD) and the Transfer Plate (TP) where the  
 772 sensor P1 is installed (Fig. 22). In the present section some of the  $\Delta Y_d$  displacements are  
 773 studied as a function of the magnetic field strength.

774 During the ramping up of the solenoid, data from some ASPDs and from short distance  
 775 measurement sensors which monitor the axial AR to LD distance were simultaneously  
 776 recorded, in the years 2008, 2009 and 2011. These data sets are shown in Figs. 23, 24  
 777 and 25, respectively. Data from other years were not taken due to the slow data-taking  
 778 cycle for the ASPDs.

779 The dots in the figures represent the measured  $\Delta Z(\text{LD}-\text{AR})$  axial motion of the Link  
 780 Disk towards the Alignment Ring as a function of the magnetic field intensity B (T).  
 781 This distance is measured using a short distance Sakae potentiometer [19]. The open  
 782 circles are the corresponding  $\Delta Y_d$  of the reconstructed Y coordinate of the L2 light spot  
 783 over the P2 sensor surface, namely, the  $\Delta Z$  motion of the TP towards the IP. At  $B_{\text{max}}$ ,  
 784 the  $\Delta Z$  motion of the TP towards the IP is smaller than the approach of the LD towards  
 785 the AR measured by the potentiometer installed at the AR (see Fig. 9). This is due to the  
 786 resistance of the Z-stops located between the endcap disks and the barrel region (see  
 787 sketch in Fig. 2). The difference is of about 3.5 mm in the three examples below. The  
 788 squares correspond to the motion of the laser beam light spot over the ASPD P5 when  
 789 crossed by the Light Path L4, indicating the relative motion between the ME/1/2 muon  
 790 chamber and the LD described at the end of the previous section. The difference in sign

791 is the result of the difference in the orientation of the local Y coordinate between the P2  
792 and the P5 sensor. At  $B_{\max}$  the measured motion is of about 3 mm.

793 The curves are all functions of the type  $a \times B^2 + b \times B + c$  fitted to the data. The fitted  
794 constants are displayed in Table 18. The uncertainties used in the fit come from the data  
795 in Table 5, and the nominal resolution of 40  $\mu\text{m}$  for the distance sensors  
796 (potentiometers).

797 The  $\chi^2/\text{NDF}$  values indicate that the uncertainties used in the fit (i.e. those of ideal  
798 environmental conditions in Table 5), were underestimated. In fact, systematic errors  
799 such as the effects of temperature, motions and possible deformations of some parts of  
800 the system were not taken into account. However, the fitted parameters to the different  
801 data points are in fair agreement with each other in the various years.

802 The different values for the NDF in the three fits in the year 2008 are due to the fact  
803 that 8 light point reconstructions over the P2 sensor crossed by the Light Path L2 and 6  
804 over the P5 sensor crossed by the Light Path L4 were of a poor quality and therefore  
805 discarded.

806

## 807 11. Summary

808 The network of laser lines and photosensors is the central feature of the CMS Link  
809 Alignment system that, in turn, is an important part of the general CMS Alignment  
810 system. The alignment provides a precise geometrical description of the detector,  
811 necessary to achieve the desired accuracy in the reconstruction of tracks from charged  
812 particles passing through an intense magnetic field.

813 The general layout of the semitransparent Amorphous Silicon Position Detectors  
814 (ASPDs), consisting of a matrix of perpendicular ZnO:Al (110 nm) strips sandwiching a  
815 layer of photosensitive Schottky photodiodes was introduced. The width of the  
816 conducting strips is 402  $\mu\text{m}$  with 22  $\mu\text{m}$  spacing between neighboring strips. The total  
817 sensitive area is approximately  $27 \times 27 \text{ mm}^2$ .

818 Prior to installation on the CMS detector, the measured performance, averaged over a  
819 sample of 122 units constructed, showed a sensor photosensitivity of  $16.3 \pm 7.6 \text{ mA/W}$ ,  
820 spatial point reconstruction resolutions of the light spot of  $\sigma_x = 5.2 \pm 2.6 \mu\text{m}$  and  $\sigma_y =$   
821  $5.1 \pm 2.4 \mu\text{m}$ , deflection angles of  $\Theta_x = -1.1 \pm 2.8 \mu\text{rad}$  and  $\Theta_y = -1.1 \pm 2.8 \mu\text{rad}$ , and a  
822 transmission of  $T = 84.8 \pm 2.9\%$ .

823 The four light path lines and the six ASPD sensors per CMS  $\Phi$  quadrant were  
824 described and details were given about the data taking procedure. The protocol to  
825 perform a full recording cycle and to reconstruct the beam spots of the 72 ASPDs  
826 installed in CMS (36 per detector side) takes slightly more than half an hour.

827 An interpretation of the motions of the beam spots on the sensor surfaces was given,  
828 presenting examples of the motions detected during some Magnet Cycles and Stability  
829 Periods after the analysis of the ASPD data recorded over the years 2008 -2013 and part  
830 of 2015, verifying the good performance of the sensors, which needed no replacements  
831 or repairs after more than seven years of operation.

832 In addition, the correlation between the CMS mechanical motions detected by the short  
833 distance measuring devices and those detected by the reconstruction of the light spots  
834 on the ASPD sensors during the ramping of the magnetic field were presented,

835 demonstrating a good agreement and, therefore, that the ASPDs data are well  
836 understood.

837 The information provided by the network of photodetectors and diode lasers is an integral part  
838 of the Link alignment system and it is used in the COCOA simulation/reconstruction software  
839 to obtain the CMS detector geometry every time the CMS structures are closed and the detector  
840 is ready for operation. The present study extend the analysis of this network using all data  
841 collected by the system, thus providing a more deep understanding on the performance of this  
842 important component of the alignment system.

843 It can be concluded that our measurements confirm that the CMS Link alignment  
844 system performed as designed, and we anticipate the future monitoring of the muon  
845 system will continue to meet all specifications.

846

#### 847 **Acknowledgments**

848 The authors thank the technical and administrative staff at CERN and all other CMS  
849 Institutes.

850 **References**

- 851 [1] The CMS Collaboration, “The CMS experiment at the CERN LHC”, JINST 3  
852 (2008) S08004.
- 853 [2] The CMS Collaboration, “The Magnet Project Technical Design Report”,  
854 CERN/LHCC 97-10.
- 855 [3] The CMS Collaboration, “The Muon Project Technical Design Report”,  
856 CERN/LHCC 97-32.
- 857 [4] The CMS Collaboration, “The Tracker Project Technical Design Report”,  
858 CERN/LHCC 98-06.
- 859 [5] V. Karimaki and G. Wrochna, CMS TN/94-199; F. Matorras and A. Meneguzzo,  
860 CMS TN/95-069 and I. Belotelov et al. CMS NOTE 2006/017.
- 861 [6] L.A. García Moral et al., Nucl. Instr. and Methods A 606 (2009) 344.
- 862 [7] P. Arce et al., Nucl. Instr. And Methods A 675 (2012) 84.
- 863 [8] P. Arce et al., Nucl. Instr. And Methods A 813 (2016) 36.
- 864 [9] M. Sobrón, “CMS detector geometry reconstructed with the Link alignment  
865 system”, PH. D. Thesis (2009), Instituto de Física de Cantabria, UC-CSIC, Santander,  
866 Spain.
- 867 [10] E. Calvo. “Characterization of mechanical properties of adhesive joints subjected  
868 to radioactive environments in particle detector alignment systems, PH. D. Thesis (2015),  
869 E.T.S. de Ingenieros Industriales y de Telecomunicación. Universidad de Cantabria,  
870 Santander, Spain.
- 871 [11] A. Calderón et al., Nucl. Instr. and Methods A 565 (2006) 603.
- 872 [12] C. Khöler et al., Nucl. Instr. and Methods A 608 (2009) 55.
- 873 [13] [A. Calderón et al., "Amorphous Silicon Position Detectors for the Link Alignment  
874 System of the CMS Detector: Users Handbook", Informe Técnico Ciemat, Madrid :  
875 CIEMAT, 2007.](#)
- 876 [14] <http://www.ciemat.es/interno/eng/instalacion/0i070.html>
- 877 [15] A. Fenyvesi et al., Z. Medizinische Physik 1 (1991) 1.
- 878 [16] J. Cárabe et al., Nucl. Instr. and Meth. A 455 (2000) 361.
- 879 [17] G. Berger, G. Ryckewaert, R. Harboe-Sorensen, and L. Adams, “CYCLONE – A  
880 Multipurpose Heavy Ion, Proton and Neutron SEE Test Site,” Abstracts for *RADEC*  
881 97 W-25, Cannes France, 1997.
- 882 [18] P. Arce and A.L. Virto, “CMS Object Oriented Code for Optical Alignment  
883 (COCOA), CMS IN 2002/060, 2002.
- 884 [19] Sakae Tsushin Kogyo Co., Ltd. - Trade Dept. 322 Ichinotsubo, Nakahara-ku,  
885 Kawasaki-city, Kanagawa-prefecture, 211-0016 Japan. ([http://www.sakae-  
887 tsushin.co.jp](http://www.sakae-<br/>886 tsushin.co.jp)).
- 888
- 889
- 890
- 891
- 892
- 893
- 894
- 895
- 896
- 897
- 898

**Figure captions**

**Fig. 1:** Longitudinal view of one quadrant of the CMS detector. Laser lines (in dashed) used for the Alignment System are shown, except for the barrel region. The position of the Z-stops is also indicated. The floor of the detector has a small inclination of about 1.23 % with respect to the gravity vector  $\mathbf{g}$  as depicted in the small drawing on the left.

**Fig. 2:** Sketch of the deformation of the endcap iron disks as a result of the compression due to the magnetic field forces and the resistance of the barrel Z-stops.

**Fig. 3:** Schematic view of the Alignment System. **Left):** one  $\Phi$  alignment plane. The continuous and dotted lines show different optical paths. **Right):** transverse view of the barrel muon detectors. The crossing lines indicate the three alignment  $\Phi$  planes with sketches of the six Modules for the Alignment of the Barrel (MABs). The CMS coordinate system is also indicated in the figure.

**Fig. 4:** Sketch of the ASPD sensor structure. The  $64 \times 64$  sensor array covers an area of  $30 \times 30 \text{ mm}^2$  including the bond pads. Fine-tuning and precise control of the optical properties and film thicknesses of the top and bottom ZnO:Al strips and of the non-patterned a-SiC:H photoconductor enable a maximum optical transmittance  $T \approx 85 \%$  at the design wavelength  $\lambda_L$  (681 nm).

**Fig. 5:** Example of the electronic equivalence of an  $8 \times 8$  strips ASPD sensor, with a sketch of the readout current distributions generated by a light spot illuminating 4 strips in each direction.

**Fig. 6:** Example of the spot signal reconstruction on the local to the sensor X (top) and Y (bottom) coordinates from the currents readout of the vertical and horizontal strips, respectively. The inset drawings show the actual readout currents from the illuminated vertical (up) and horizontal (down) strips.

**Fig. 7:** The photograph on the left shows the sensor carrier board with place for sensor accommodation and two perpendicular lines of 64 aluminium terminated pads for sensor electronics bonding. Also visible are the “horizontal” and “vertical” boards of the ASPD FE electronics, with their various components: resistors, capacitors, the 16:1 multiplexers and the “male” miniature connectors to extract the signals. The photograph on the right shows the final compact form, whose dimensions are:  $4.7 \times 4.7 \times 4.7 \text{ cm}^3$ .

**Fig. 8:** **a)** Diagram of the LEB readout card showing the various integrated blocks: Bus Interface (BI), CAN bus Interface (CI), ASPD Control Interface (ACI), ASPD Signal Conditioner (ASC), Micro Controller Units (MCU), Fault Injection board Interface (FI) and the Programming Interface (PI). **b)** Photograph of a Local Electronic Board (LEB) where the blocks described in the text and in the diagram in a) are installed.

**Fig. 9:** Sketch of main Link Alignment elements (R-Z view, not to scale) in a quadrant of a  $\Phi$  plane. The inset drawing shows the  $R\phi$  projection of the Link System in the vicinity of the external MAB, showing the two Light Lines emerging from the Link Disk collimator.

**Fig. 10:** Labelling of the four laser lines (L1 to L4) and the six ASPD (P1 to P6) sensors in a  $\Phi$  link alignment quadrant. For each measurement, the three lasers are successively turned on.

**Fig. 11:** Sketch of a Laser Box (LB) and its operation mode.

**Fig. 12:** Sketch of **a)** an external MAB with the location of the tiltmeter inside the Laser Level and **b)** the Laser Level (LL) mechanical structure containing one tiltmeter and one collimator.

**Fig. 13:** Photograph of an ASPD sensor with its local axis system of coordinates and one example of possible incoming beam direction.

**Fig. 14:** Distribution of the (X, Y) reconstructed coordinates, at  $\Phi=+75^\circ$ , of the 23 recorded ASPD events during the SP1 of the 2008 CMS operation. Rows correspond to the four laser lines, columns correspond to the sequentially crossed ASPD sensors.

**Fig. 15:** Distribution of the (X, Y) reconstructed coordinates, at  $\Phi=+75^\circ$ , of the 15 recorded ASPD events during the SP6 of the 2009 CMS operation. Rows correspond to the four laser lines, columns correspond to the sequentially crossed ASPD sensors.

**Fig. 16:** Distribution of the (X, Y) reconstructed coordinates, at  $\Phi=+75^\circ$ , of the 44 recorded ASPD events during the SP1 of the 2010 CMS operation. Rows correspond to the four laser lines, columns correspond to the sequentially crossed ASPD sensors.

**Fig. 17:** Distribution of the (X, Y) reconstructed coordinates, at  $\Phi=+75^\circ$ , of the 46 recorded ASPD events during the SP2 of the 2011 CMS operation. Rows correspond to the four laser lines, columns correspond to the sequentially crossed ASPD sensors..

**Fig. 18:** Distribution of the (X, Y) reconstructed coordinates, at  $\Phi=+75^\circ$ , of the 187 recorded ASPD events during the SP2 of the 2012 CMS operation. Rows correspond to the four laser lines, columns correspond to the sequentially crossed ASPD sensors.

**Fig. 19:** Distribution of the (X, Y) reconstructed coordinates, at  $\Phi=+75^\circ$ , of the 64 recorded ASPD events during the SP1 of the 2013 CMS operation. Rows correspond to the four laser lines, columns correspond to the sequentially crossed ASPD sensors..

**Fig. 20:** Distribution of the (X, Y) reconstructed coordinates, at  $\Phi=+75^\circ$ , of the 30 recorded ASPD events during the SP1 of the 2015 CMS operation. Rows correspond to the four laser lines, columns correspond to the sequentially crossed ASPD sensors..

**Fig. 21:** Geometrical distance,  $d_i$ , between the reconstructed  $(x_i, y_i)$  coordinates of the light spot number  $i$  and the first  $(x_o, y_o)$  light spot on a given sensor  $P$  of a given laser line in the Stability Period under study. The origin of coordinates is the point  $(0, 0)$  of the sensor's active area. The reference  $(x_o, y_o)$  coordinates (inside the sensor surface) is irrelevant.

**Fig. 22:** Drawing of the Transfer Plate at the  $\Phi = +75^\circ$  quadrant. The left straight line represents the Light Path L4 crossing ASPD P4. The right straight line corresponds either to L2 or L3 Light Paths crossing ASPD P1. Lines are parallel and about 5 cm apart from each other.

**Fig. 23:** During ramp up in magnet intensity in 2008: motion  $\Delta Z(\text{LD-AR})$  (dots),  $\Delta Z(\text{LD\&TP})$  with respect to the Interaction Point as seen from P2 in the laser path L2 (circles) and motion of ME/1/2 with respect to LD as seen from P5 in the laser path L4 (squares).

**Fig. 24:** During rump up in magnet intensity in 2009: motion  $\Delta Z(\text{LD-AR})$  (dots),  $\Delta Z(\text{LD\&TP})$  with respect to the Interaction Point as seen from P2 in the laser path L2

(circles) and motion of ME/1/2 with respect to LD as seen from P5 in the laser path L4 (squares).

**Fig. 25:** During rump up in magnet intensity in 2011: motion  $\Delta Z(\text{LD-AR})$  (dots),  $\Delta Z(\text{LD\&TP})$  with respect to the Interaction Point as seen from P2 in the laser path L2 (circles) and motion of ME/1/2 with respect to LD as seen from P5 in the laser path L4 (squares).

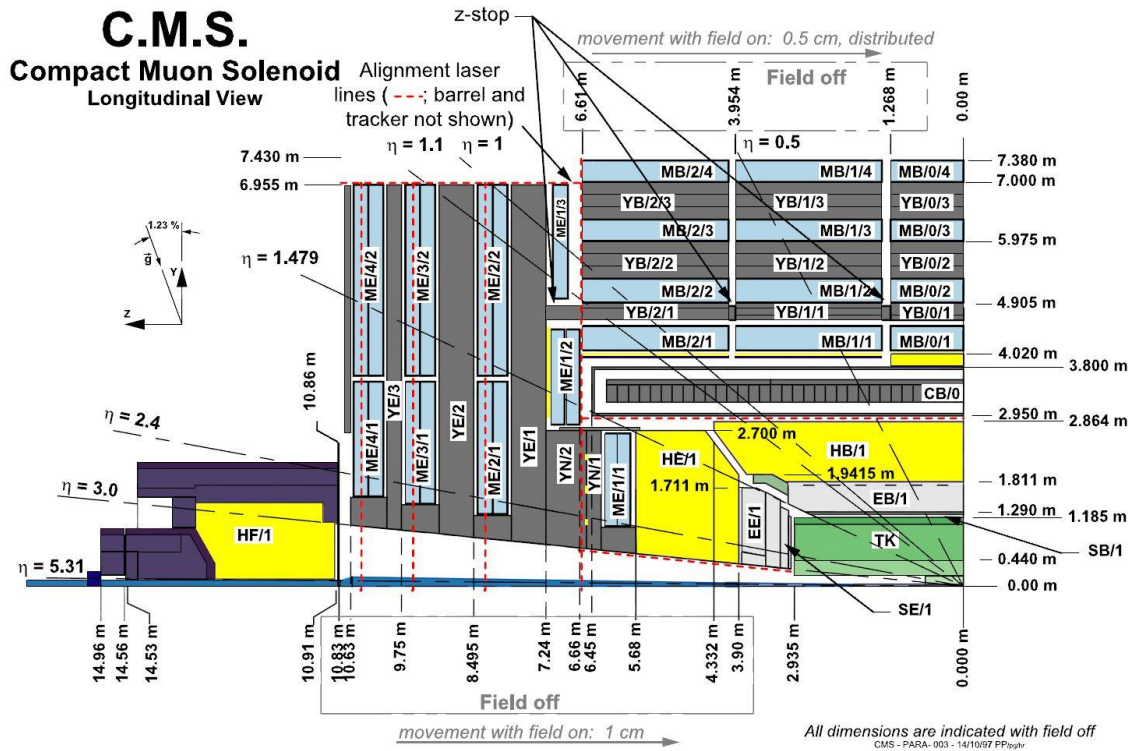


**Fig. 1:** Longitudinal view of one quadrant of the CMS detector. Laser lines (in dashed) used for the Alignment System are shown, except for the barrel region. The position of the Z-stops is also indicated. The floor of the detector has a small inclination of about 1.23 % with respect to the gravity vector  $g$  as depicted in the small drawing on the left.

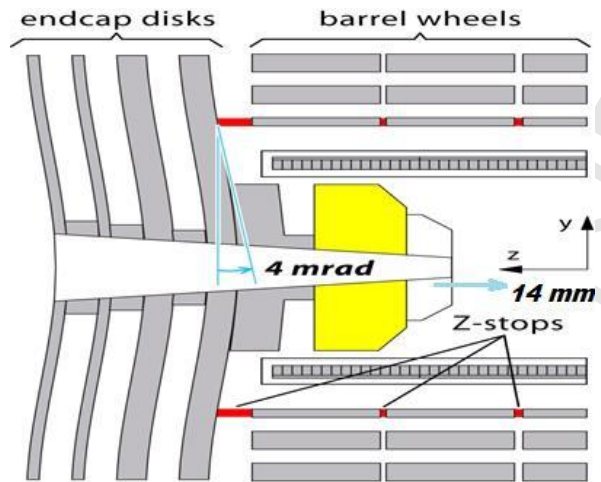


**Fig. 2:** Sketch of the deformation of the endcap iron disks as a result of the compression due to the magnetic field forces and the resistance of the barrel Z-stops.

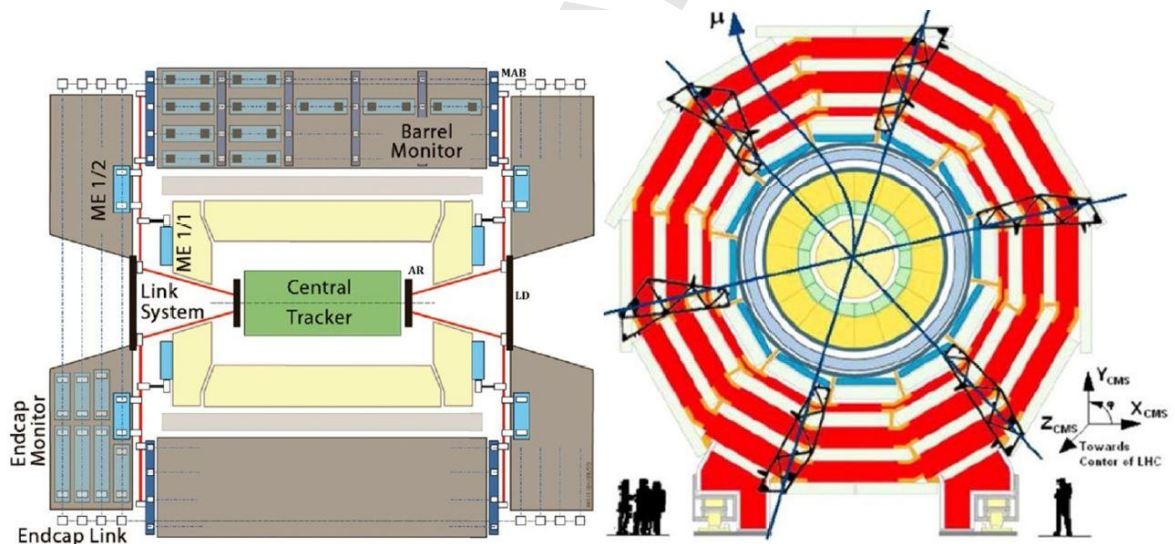


**Fig. 3:** Schematic view of the Alignment System. *Left*): one  $\Phi$  alignment plane. The continuous and dotted lines show different optical paths. *Right*): transverse view of the barrel muon detectors. The crossing lines indicate the three alignment  $\Phi$  planes with sketches of the six Modules for the Alignment of the Barrel (MABs). The CMS coordinate system is also indicated in the figure.

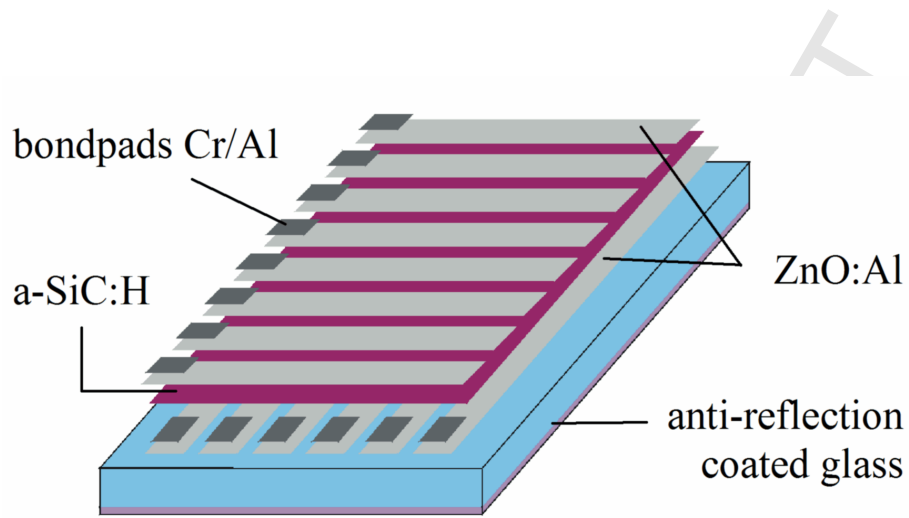


**Fig. 4:** Sketch of the ASPD sensor structure. The  $64 \times 64$  sensor array covers an area of  $30 \times 30 \text{ mm}^2$  including the bond pads. Fine-tuning and precise control of the optical properties and film thicknesses of the top and bottom ZnO:Al strips and of the non-patterned a-SiC:H photoconductor enable a maximum optical transmittance  $T \approx 85 \%$  at the design wavelength  $\lambda_L$  (681 nm).

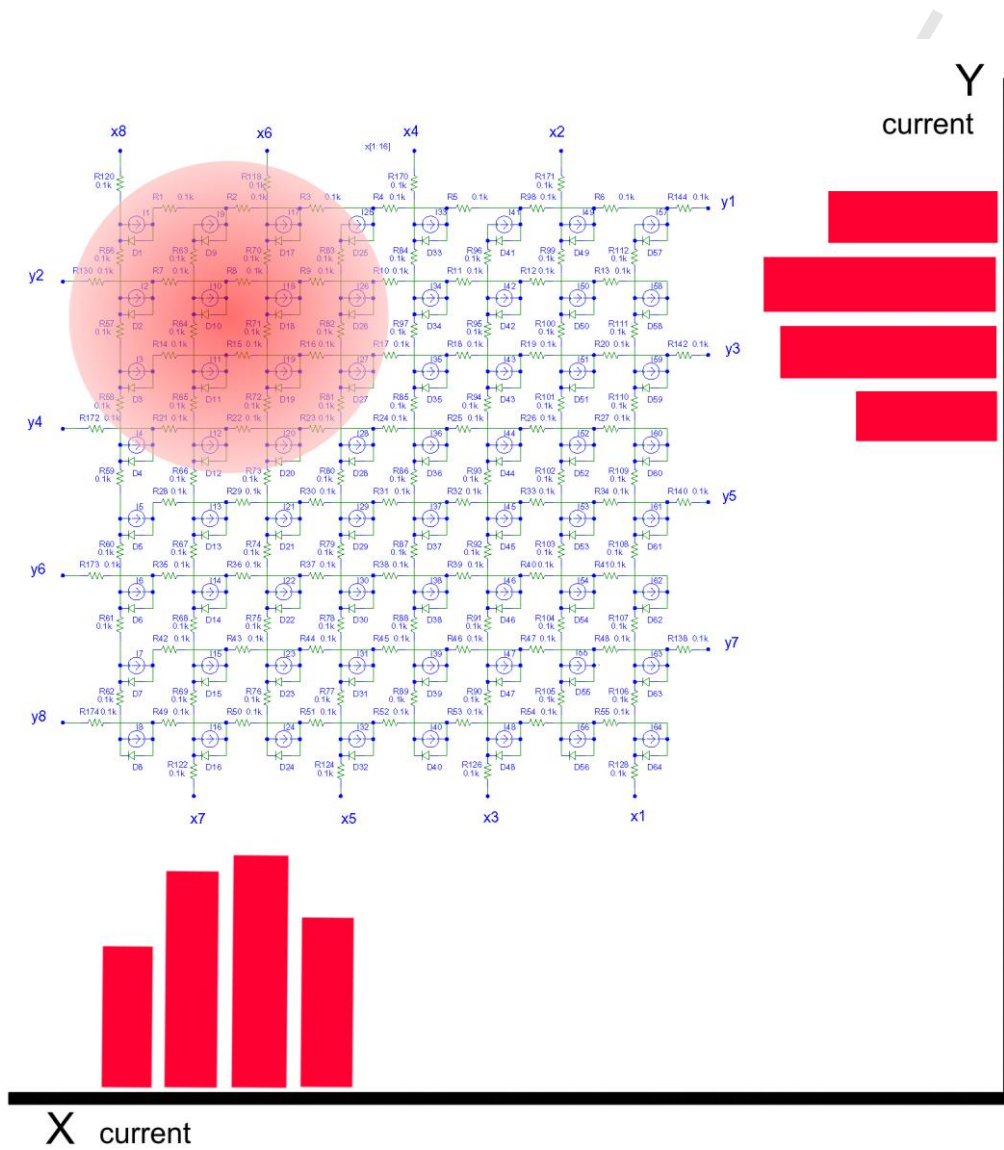


**Fig. 5:** Example of the electronic equivalence of an 8 x 8 strips ASPD sensor, with a sketch of the readout current distributions generated by a light spot illuminating 4 strips in each direction.

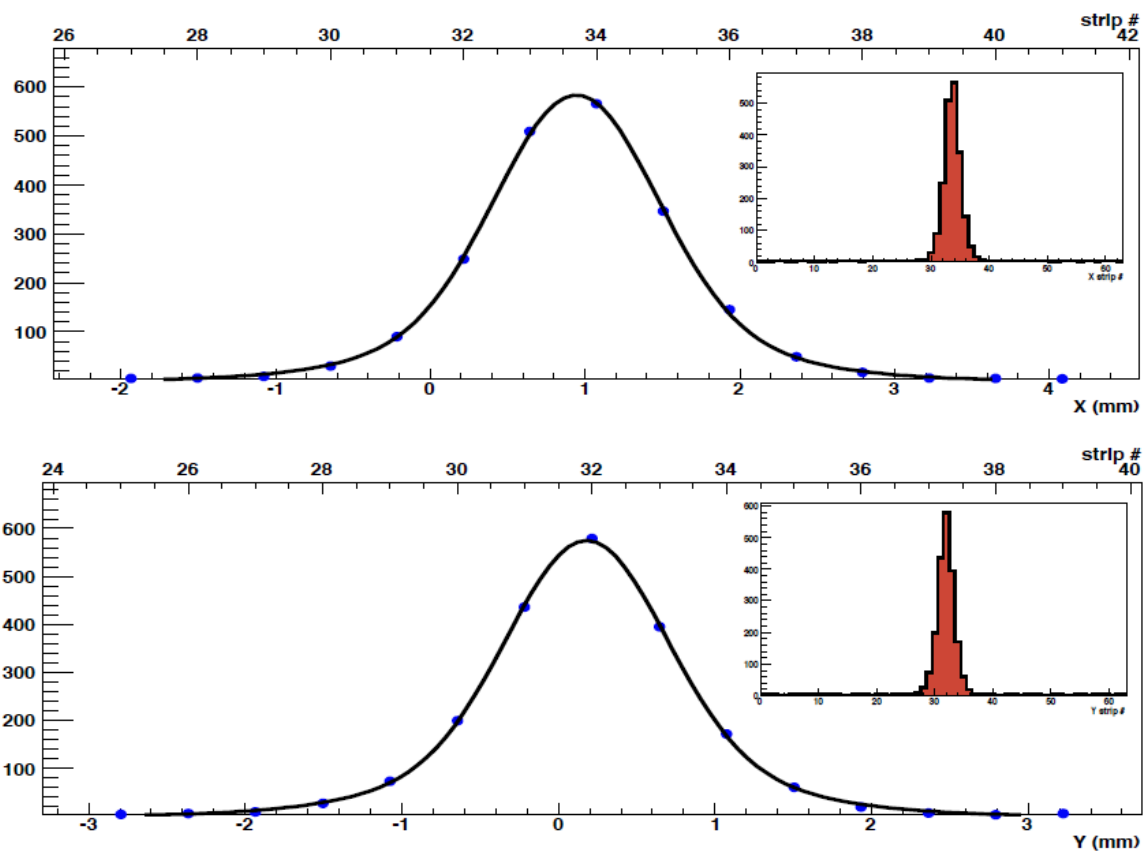


**Fig. 6:** Example of the spot signal reconstruction on the local to the sensor X (top) and Y (bottom) coordinates from the currents readout of the vertical and horizontal strips, respectively. The inset drawings show the actual readout currents from the illuminated vertical (up) and horizontal (down) strips.

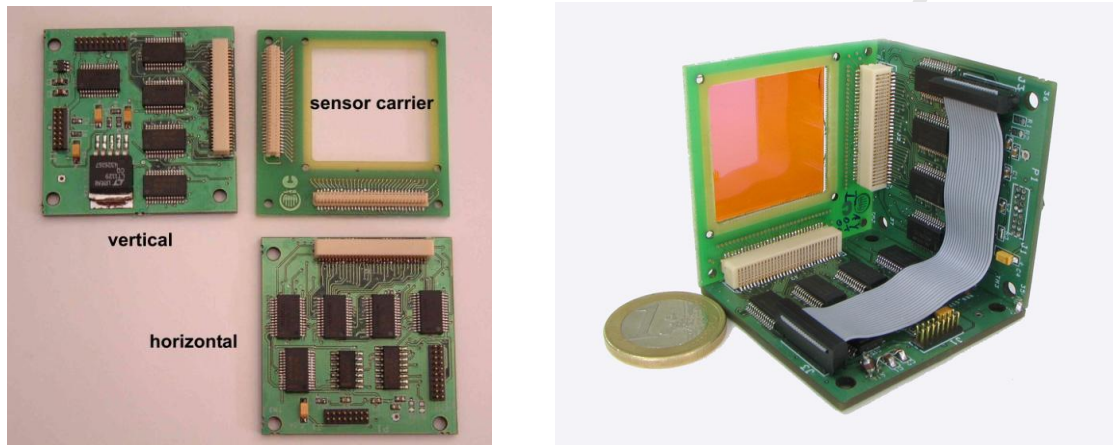
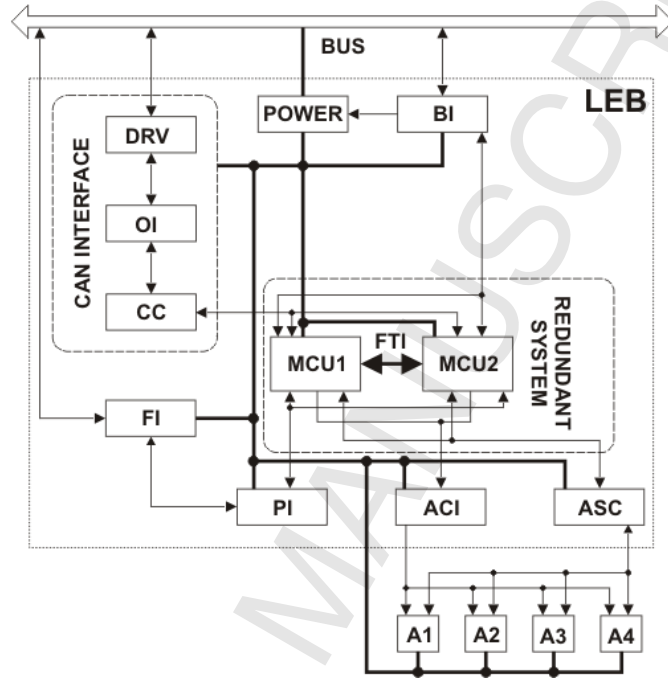


**Fig. 7:** The photograph on the left shows the sensor carrier board with place for sensor accommodation and two perpendicular lines of 64 aluminium terminated pads for sensor electronics bonding. Also visible are the “horizontal” and “vertical” boards of the ASPD FE electronics, with their various components: resistors, capacitors, the 16:1 multiplexers and the “male” miniature connectors to extract the signals. The photograph on the right shows the final compact form, whose dimensions are:  $4.7 \times 4.7 \times 4.7 \text{ cm}^3$ .

a)



b)

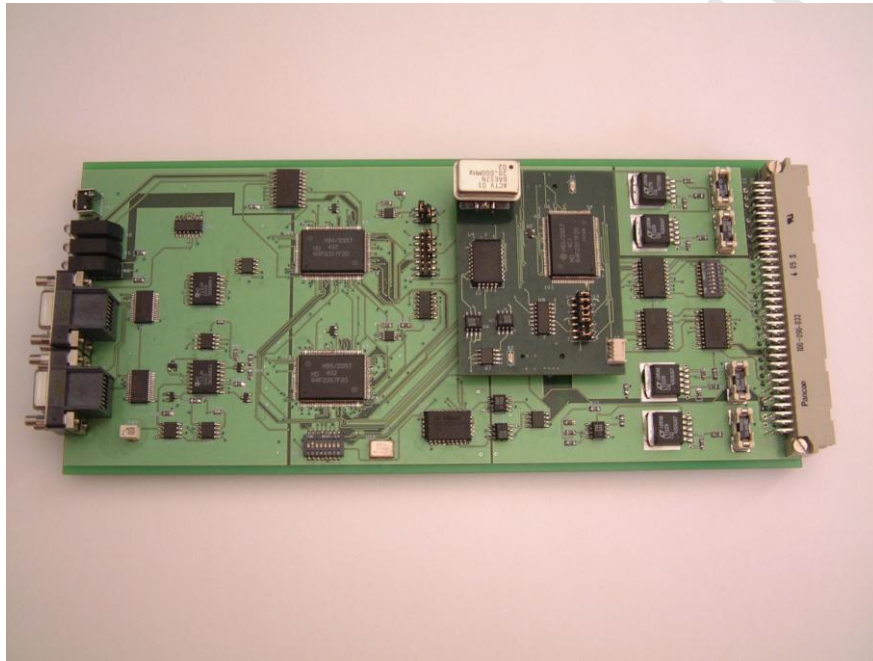


**Fig. 8:** *a) Diagram of the LEB readout card showing the various integrated blocks: Bus Interface (BI), CAN bus Interface (CI), ASPD Control Interface (ACI), ASPD Signal Conditioner (ASC), Micro Controller Units (MCU), Fault Injection board Interface (FI) and the Programming Interface (PI). b) Photograph of a Local Electronic Board (LEB) where the blocks described in the text and in the diagram in a) are installed.*

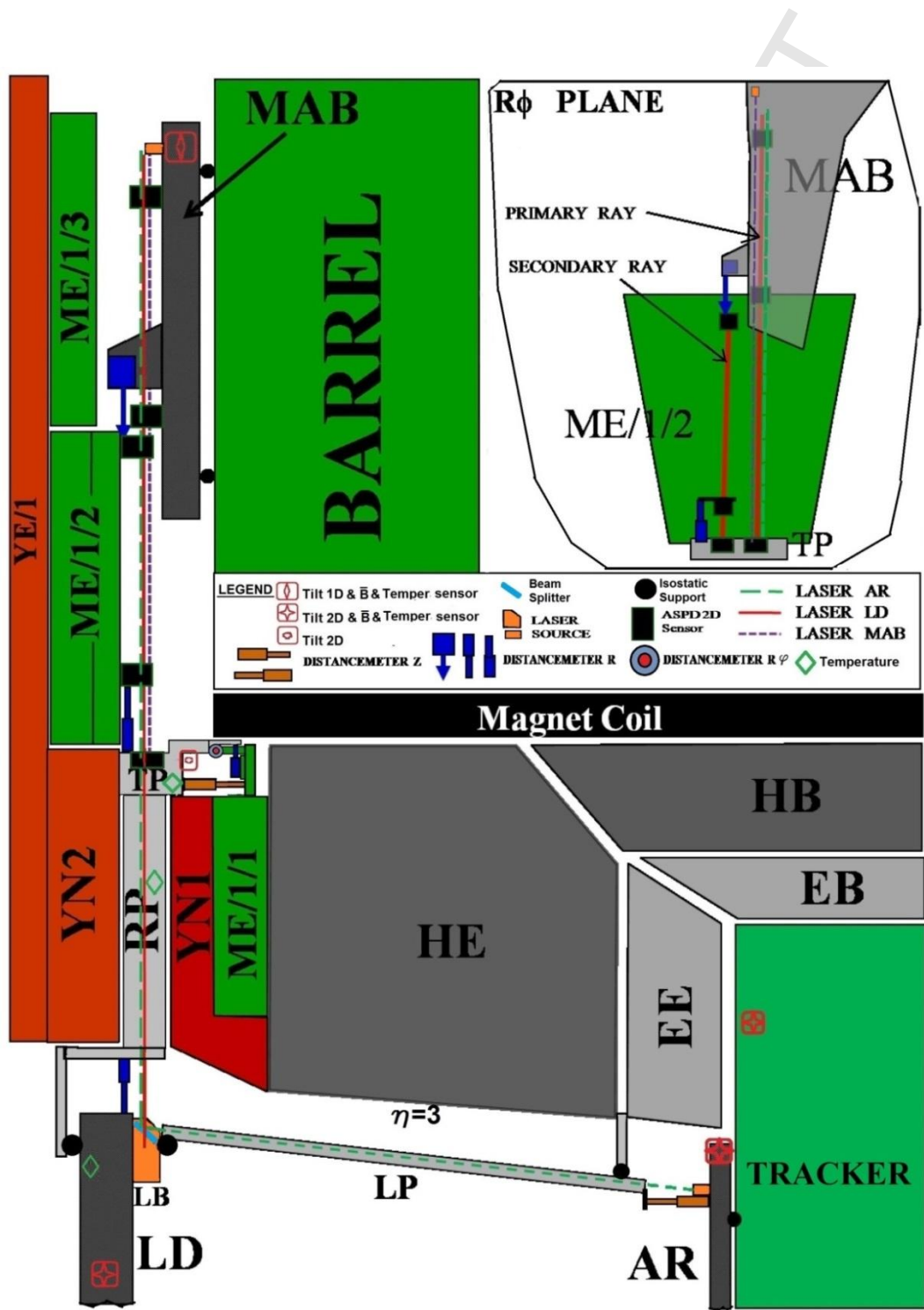


**Fig. 9:** Sketch of main Link Alignment elements ( $R$ - $Z$  view, not to scale) in a quadrant of a  $\Phi$  plane. The inset drawing shows the  $R\phi$  projection of the Link System in the vicinity of the external MAB, showing the two Light Lines emerging from the Link Disk collimator.

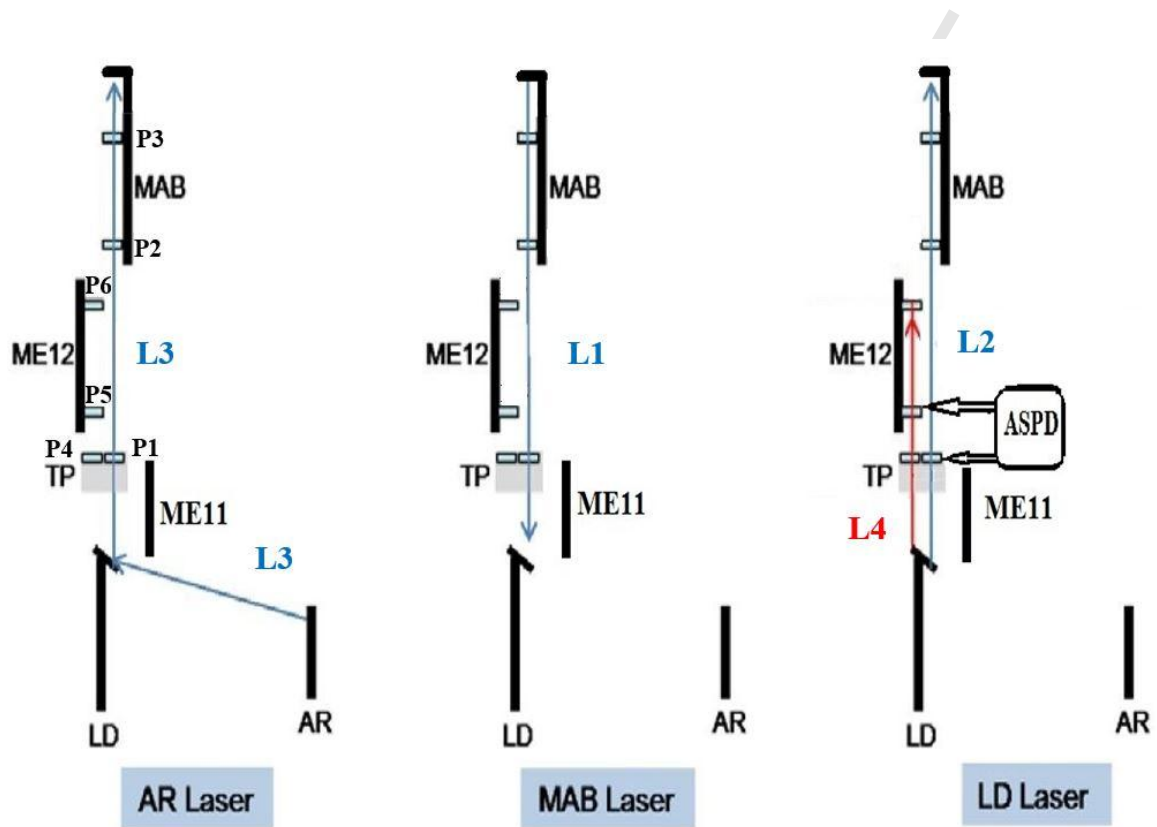


**Fig. 10:** Labelling of the four laser lines (L1 to L4) and the six ASPD (P1 to P6) sensors in a  $\Phi$  link alignment quadrant. For each measurement, the three lasers are successively turned on.

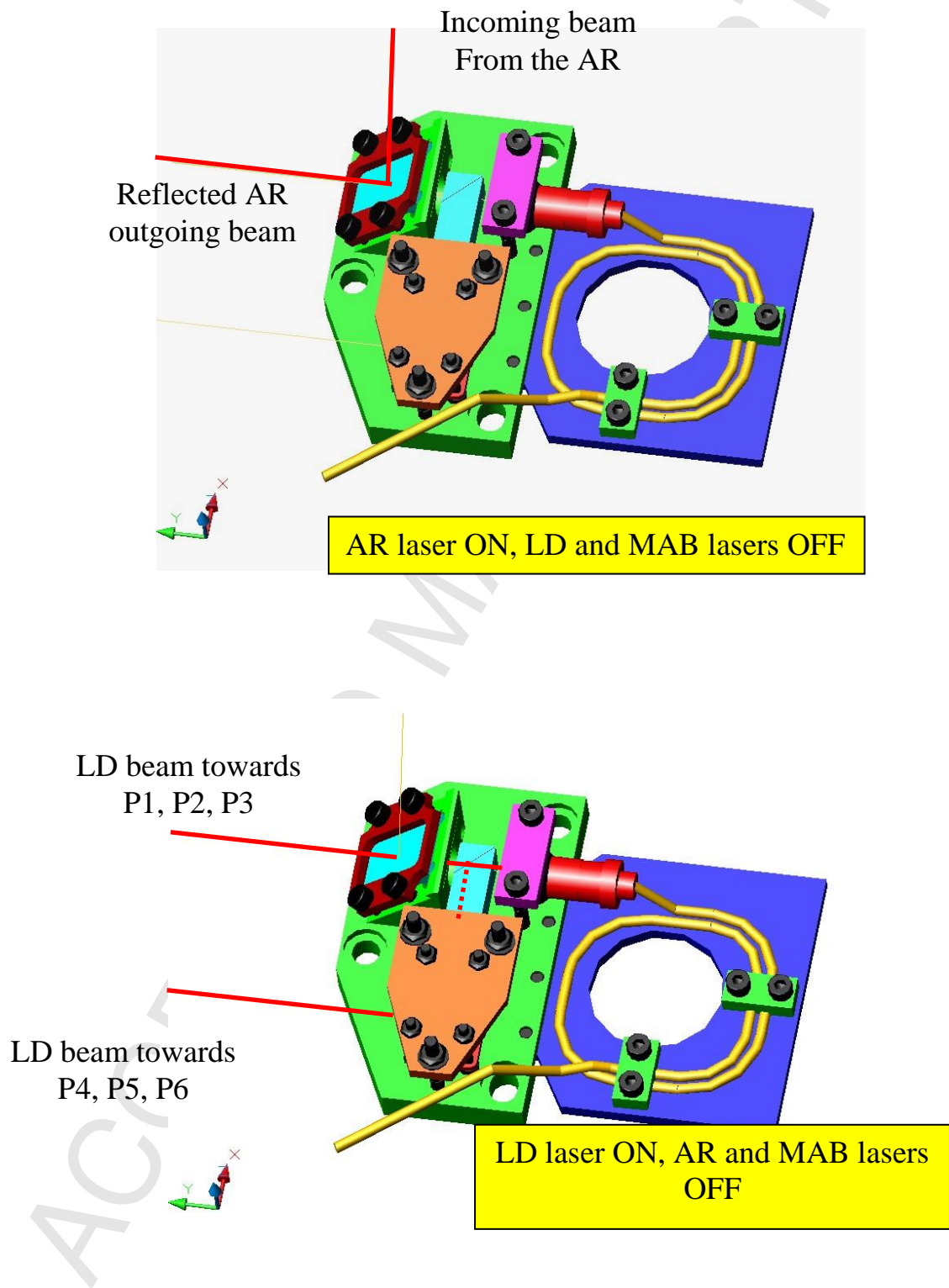


**Fig. 11:** Sketch of a Laser Box (LB) and its operation mode.

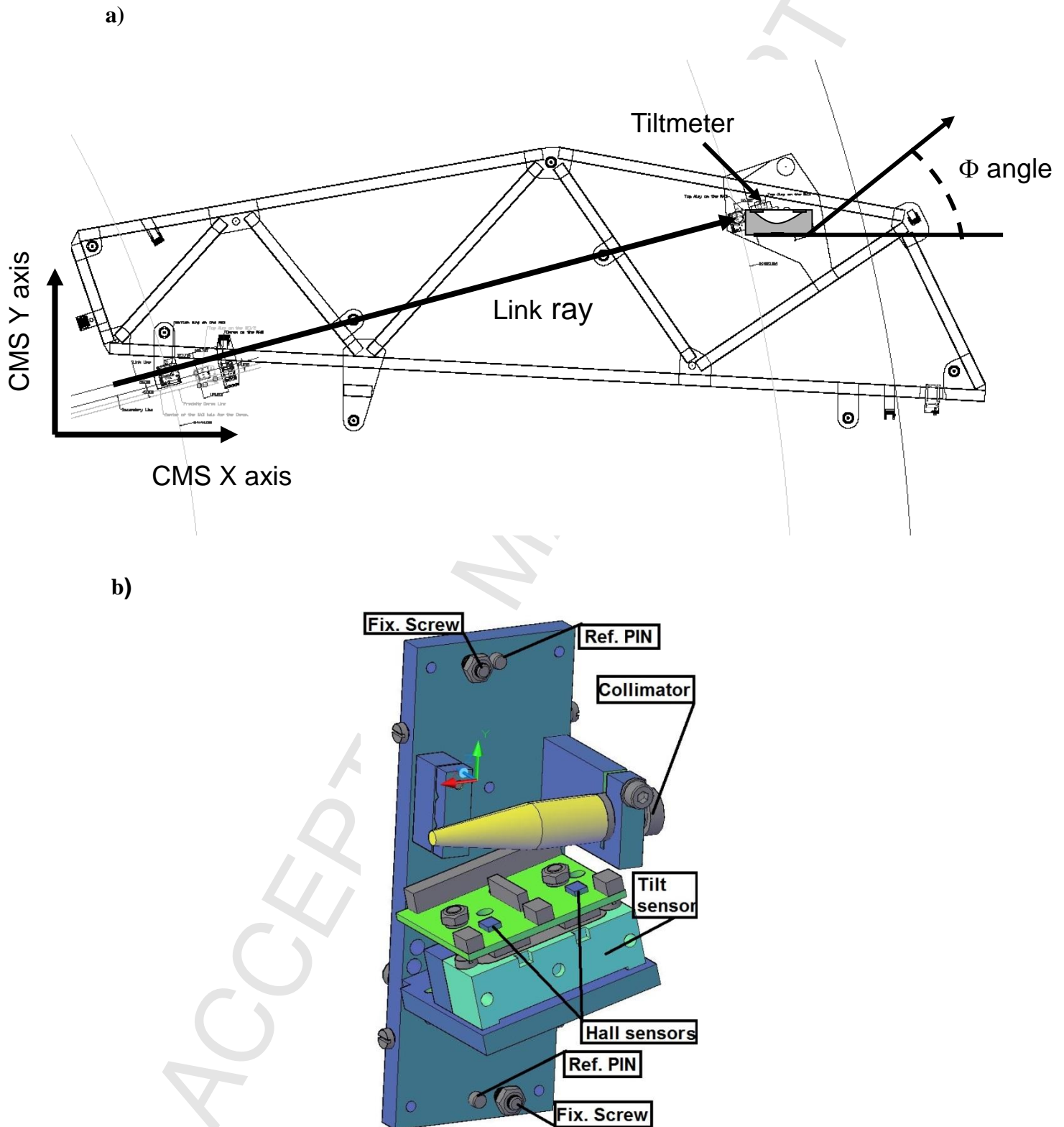


**Fig. 12:** Sketch of **a)** an external MAB with the location of the tiltmeter inside the Laser Level and **b)** the Laser Level (LL) mechanical structure containing one tiltmeter and one collimator.

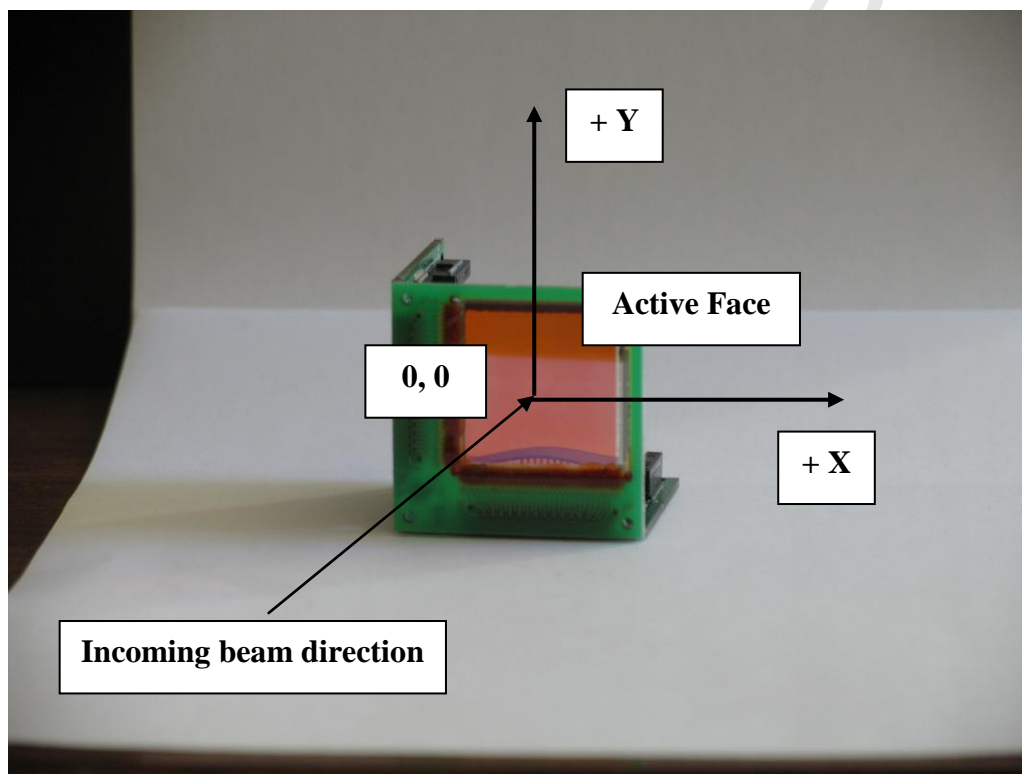


**Fig. 13:** Photograph of an ASPD sensor with its local axis system of coordinates and one example of possible incoming beam direction.

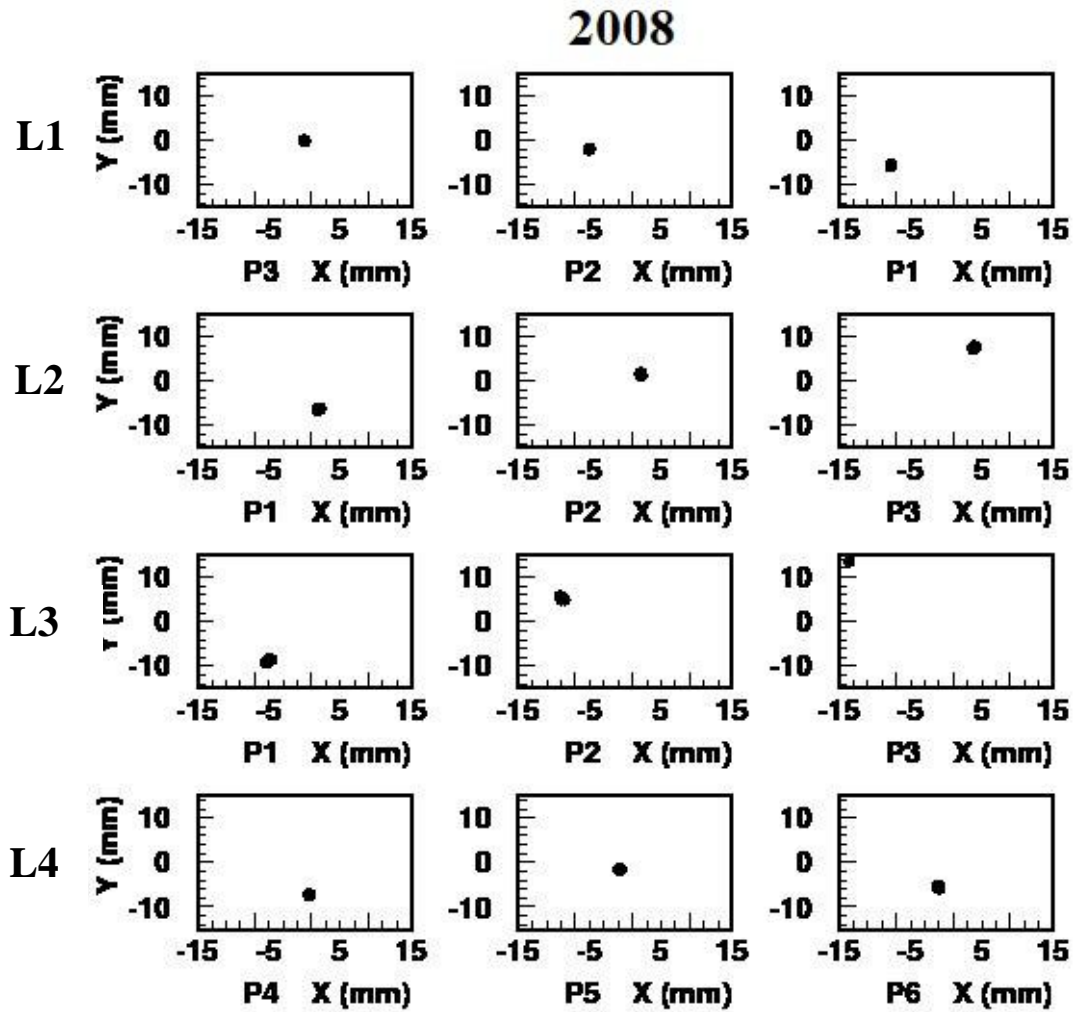


**Fig. 14:** Distribution of the  $(X, Y)$  reconstructed coordinates, at  $\Phi=+75^\circ$ , of the 23 recorded ASPD events during the SP1 of the 2008 CMS operation. Rows correspond to the four laser lines, columns correspond to the sequentially crossed ASPD sensors.

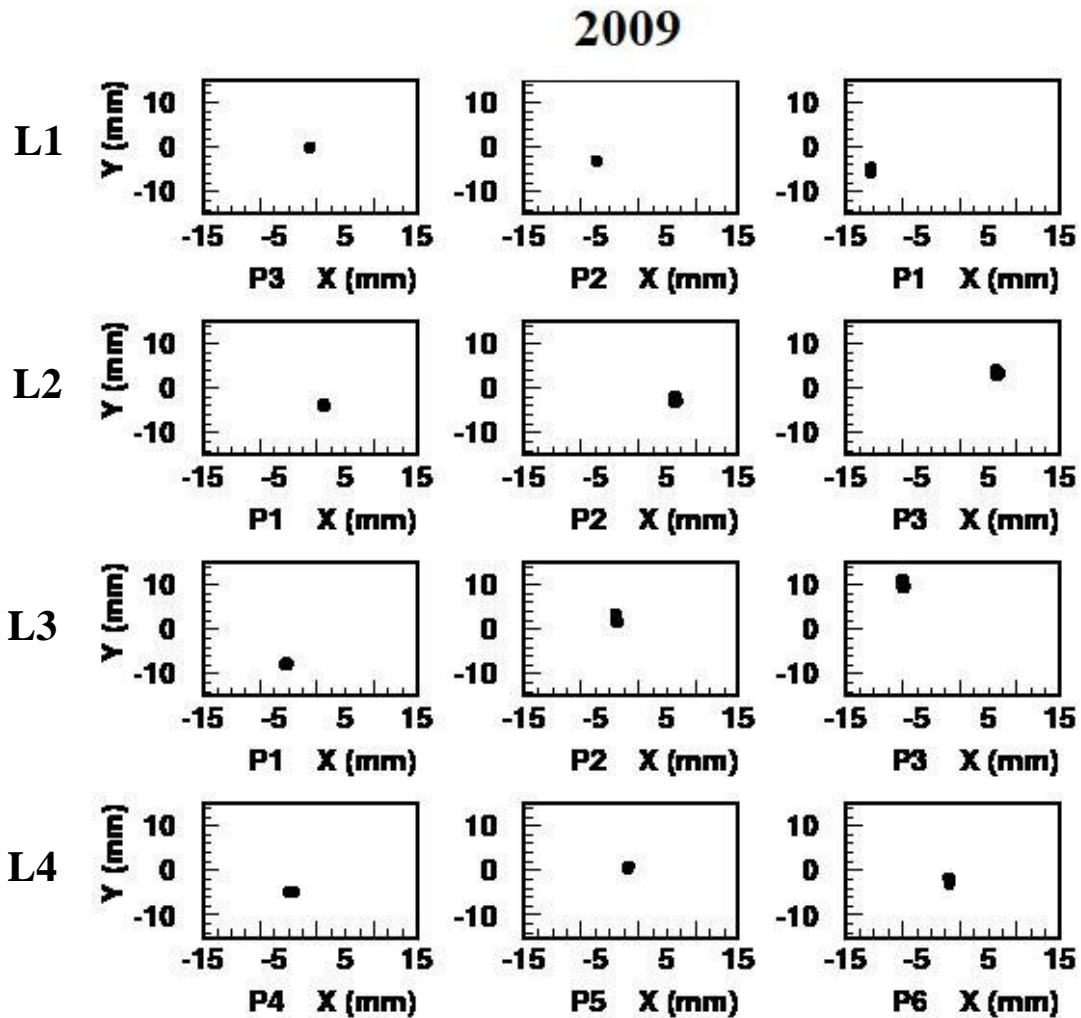


**Fig. 15:** Distribution of the  $(X, Y)$  reconstructed coordinates, at  $\Phi=+75^\circ$ , of the 15 recorded ASPD events during the SP6 of the 2009 CMS operation. Rows correspond to the four laser lines, columns correspond to the sequentially crossed ASPD sensors.

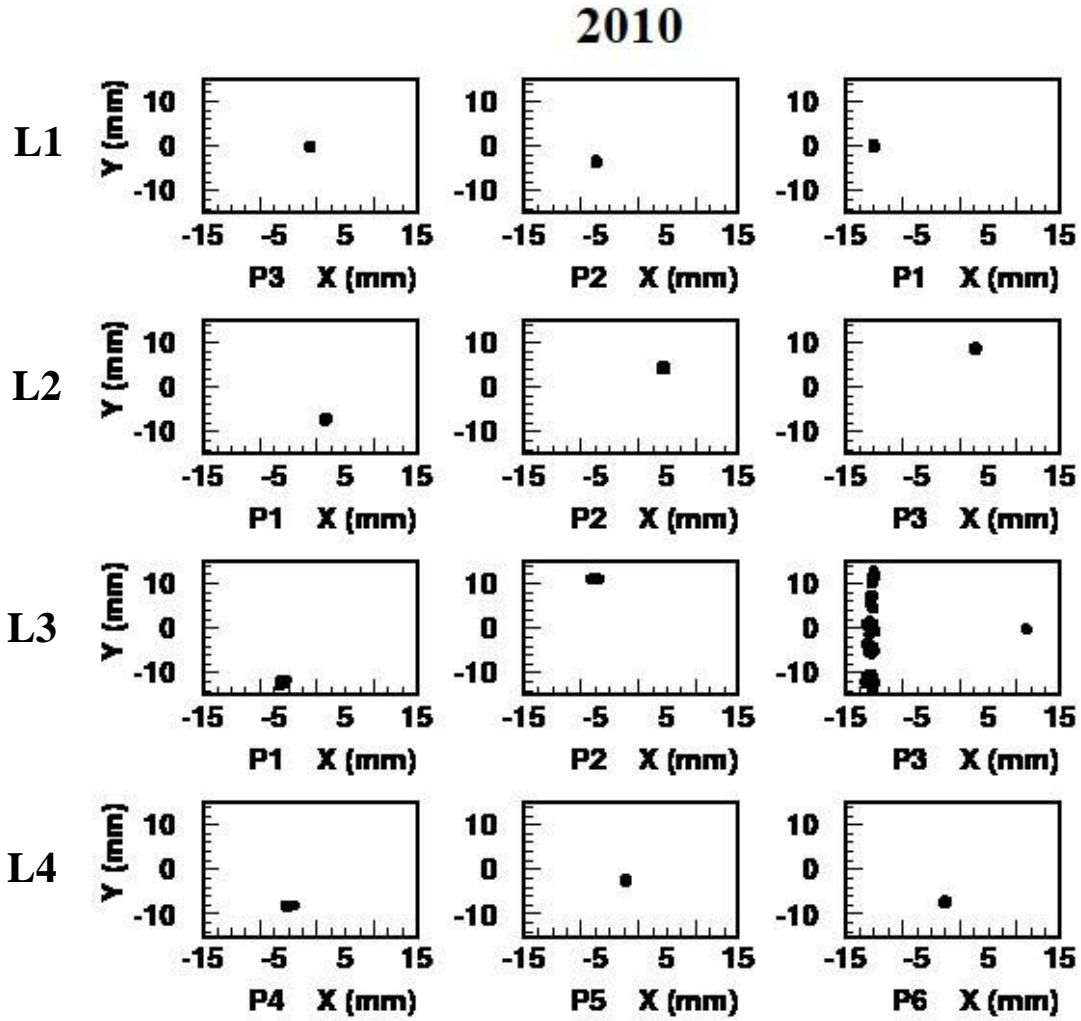


**Fig. 16:** Distribution of the  $(X, Y)$  reconstructed coordinates, at  $\Phi=+75^\circ$ , of the 44 recorded ASPD events during the SP1 of the 2010 CMS operation. Rows correspond to the four laser lines, columns correspond to the sequentially crossed ASPD sensors.

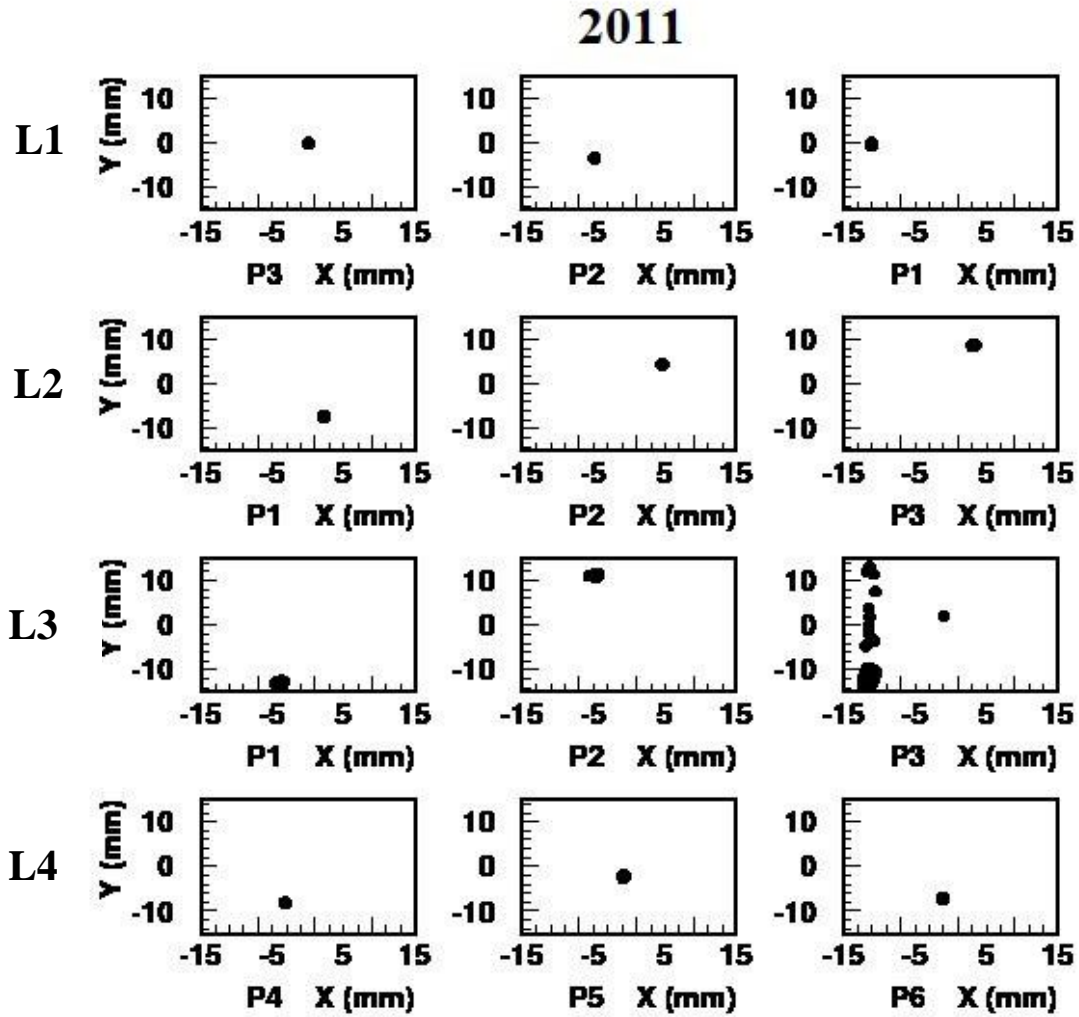


**Fig. 17:** Distribution of the  $(X, Y)$  reconstructed coordinates, at  $\Phi=+75^\circ$ , of the 46 recorded ASPD events during the SP2 of the 2011 CMS operation. Rows correspond to the four laser lines, columns correspond to the sequentially crossed ASPD sensors.

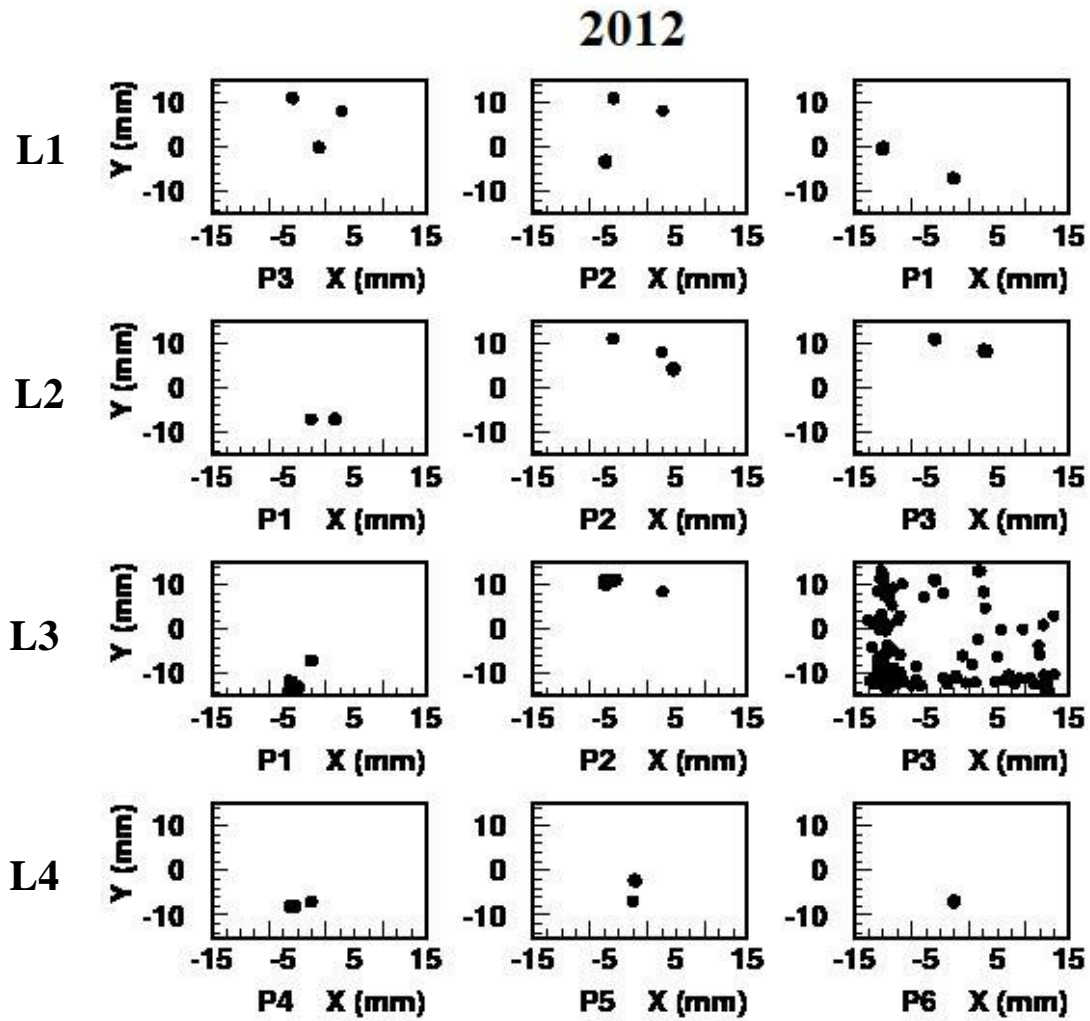


**Fig. 18:** Distribution of the  $(X, Y)$  reconstructed coordinates, at  $\Phi=+75^\circ$ , of the 187 recorded ASPD events during the SP2 of the 2012 CMS operation. Rows correspond to the four laser lines, columns correspond to the sequentially crossed ASPD sensors.

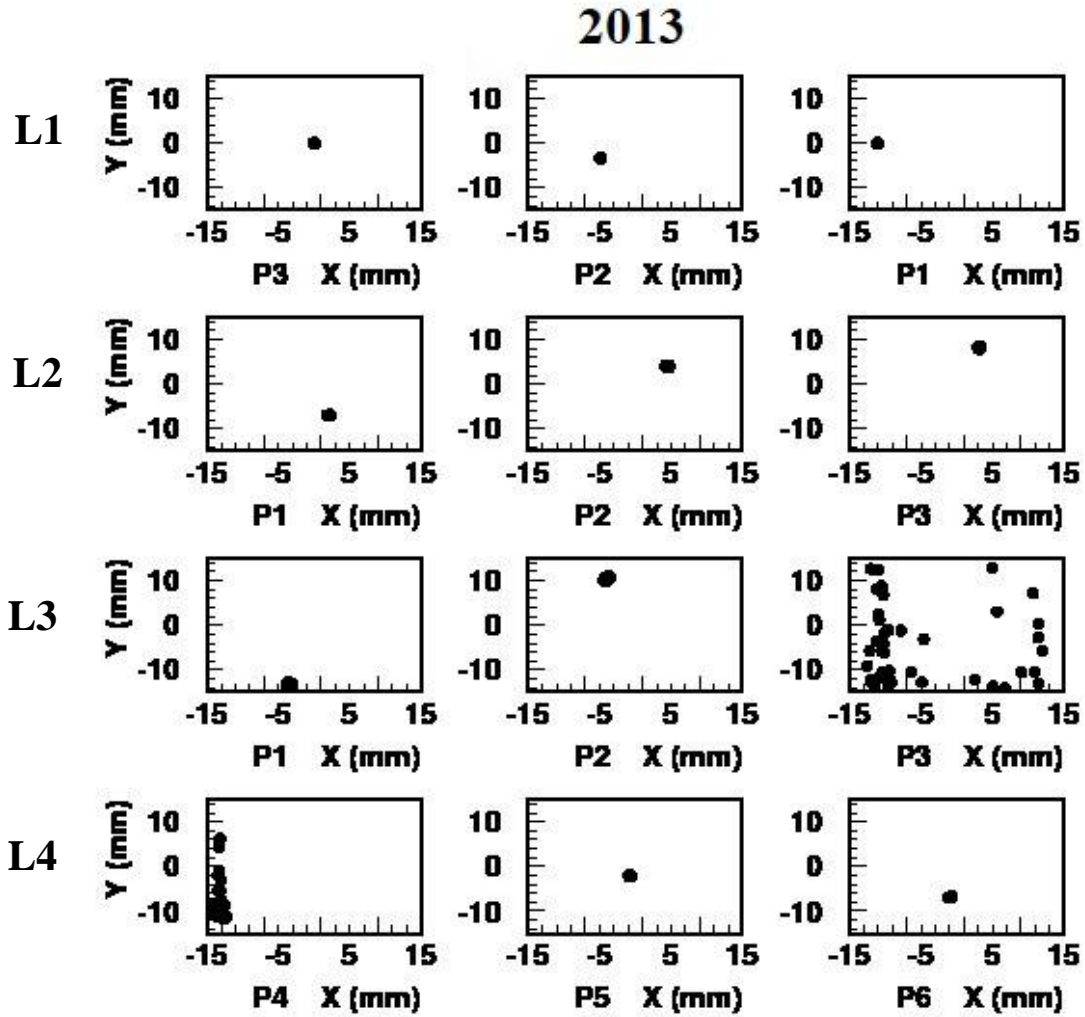


**Fig. 19:** Distribution of the  $(X, Y)$  reconstructed coordinates, at  $\Phi=+75^\circ$ , of the 64 recorded ASPD events during the SP1 of the 2013 CMS operation. Rows correspond to the four laser lines, columns correspond to the sequentially crossed ASPD sensors.

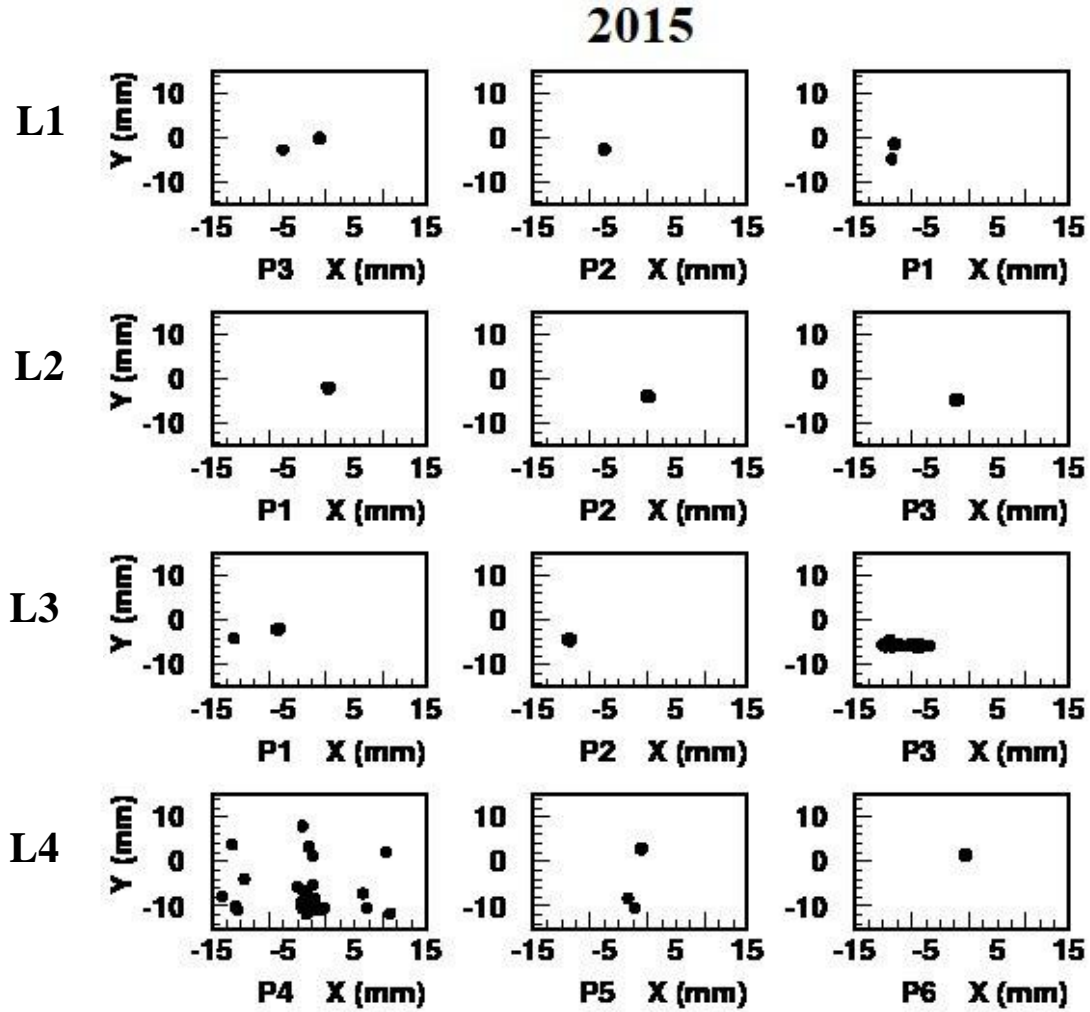


**Fig. 20:** Distribution of the  $(X, Y)$  reconstructed coordinates, at  $\Phi=+75^\circ$ , of the 30 recorded ASPD events during the SP1 of the 2015 CMS operation. Rows correspond to the four laser lines, columns correspond to the sequentially crossed ASPD sensors.

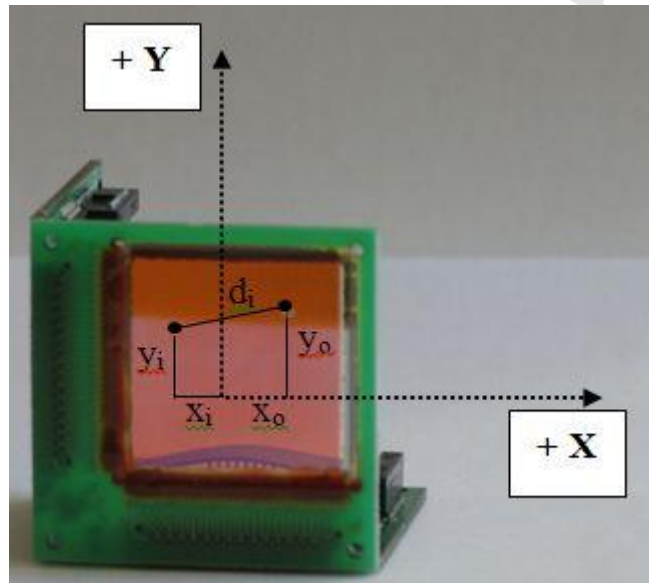


**Fig. 21:** Geometrical distance,  $d_i$ , between the reconstructed  $(x_i, y_i)$  coordinates of the light spot number  $i$  and the first  $(x_o, y_o)$  light spot on a given sensor  $P$  of a given laser line in the Stability Period under study. The origin of coordinates is the point  $(0, 0)$  of the sensor's active area. The reference  $(x_o, y_o)$  coordinates (inside the sensor surface) is irrelevant.

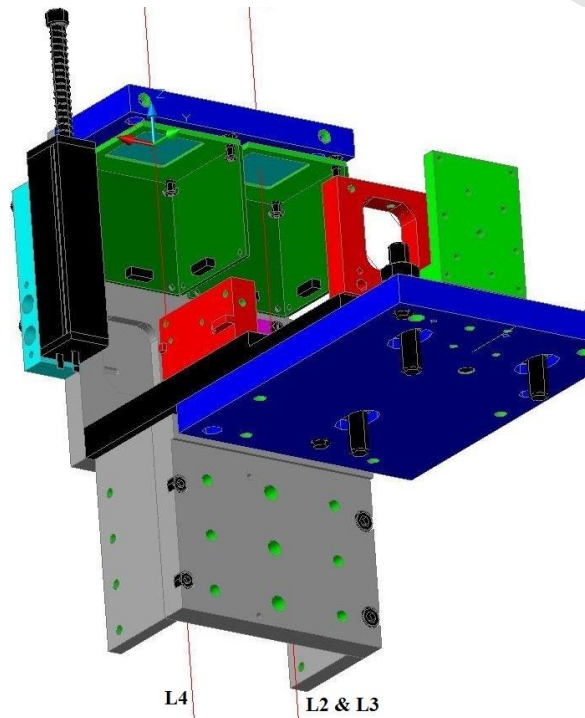


**Fig. 22:** Drawing of the Transfer Plate at the  $\Phi = +75^\circ$  quadrant. The left straight line represents the Light Path L4 crossing ASPD P4. The right straight line corresponds either to L2 or L3 Light Paths crossing ASPD P1. Lines are parallel and about 5 cm apart from each other.

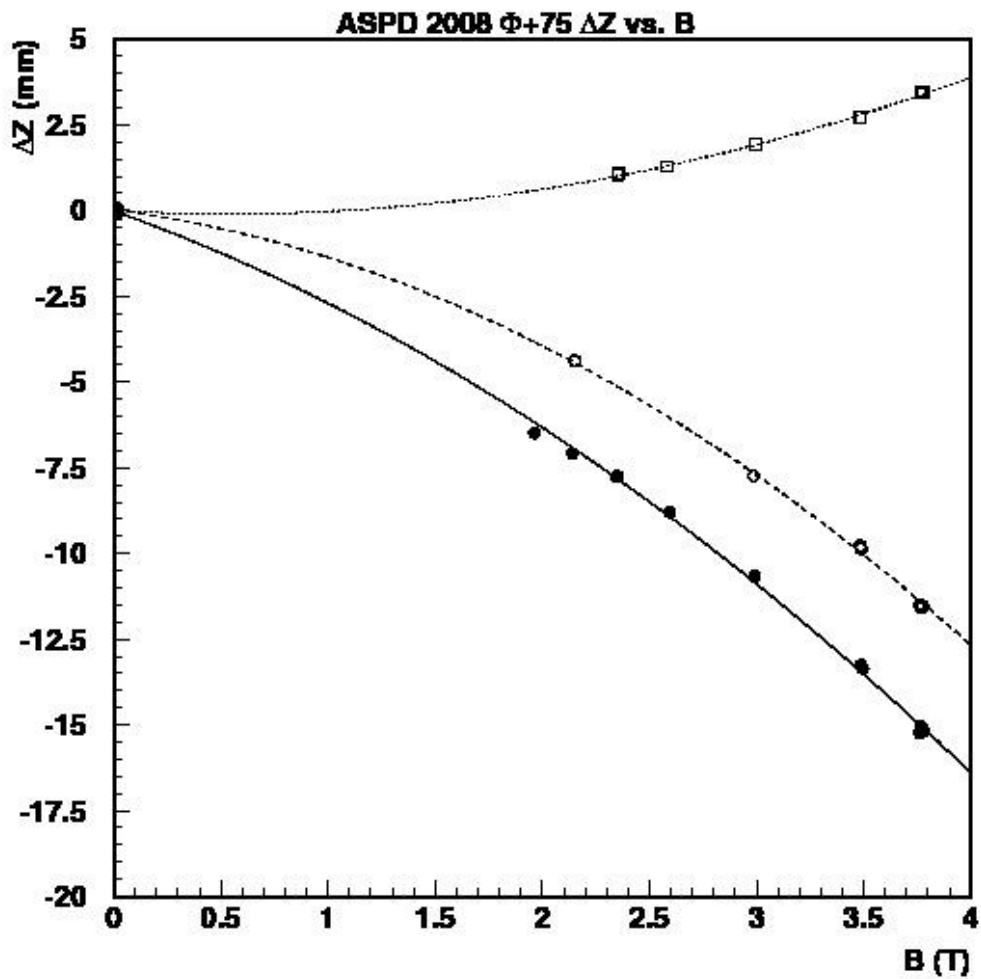


**Fig. 23:** During ramp up in magnet intensity in 2008: motion  $\Delta Z$ (LD-AR) (dots),  $\Delta Z$ (LD&TP) with respect to the Interaction Point as seen from P2 in the laser path L2 (circles) and motion of ME/1/2 with respect to LD as seen from P5 in the laser path L4 (squares).

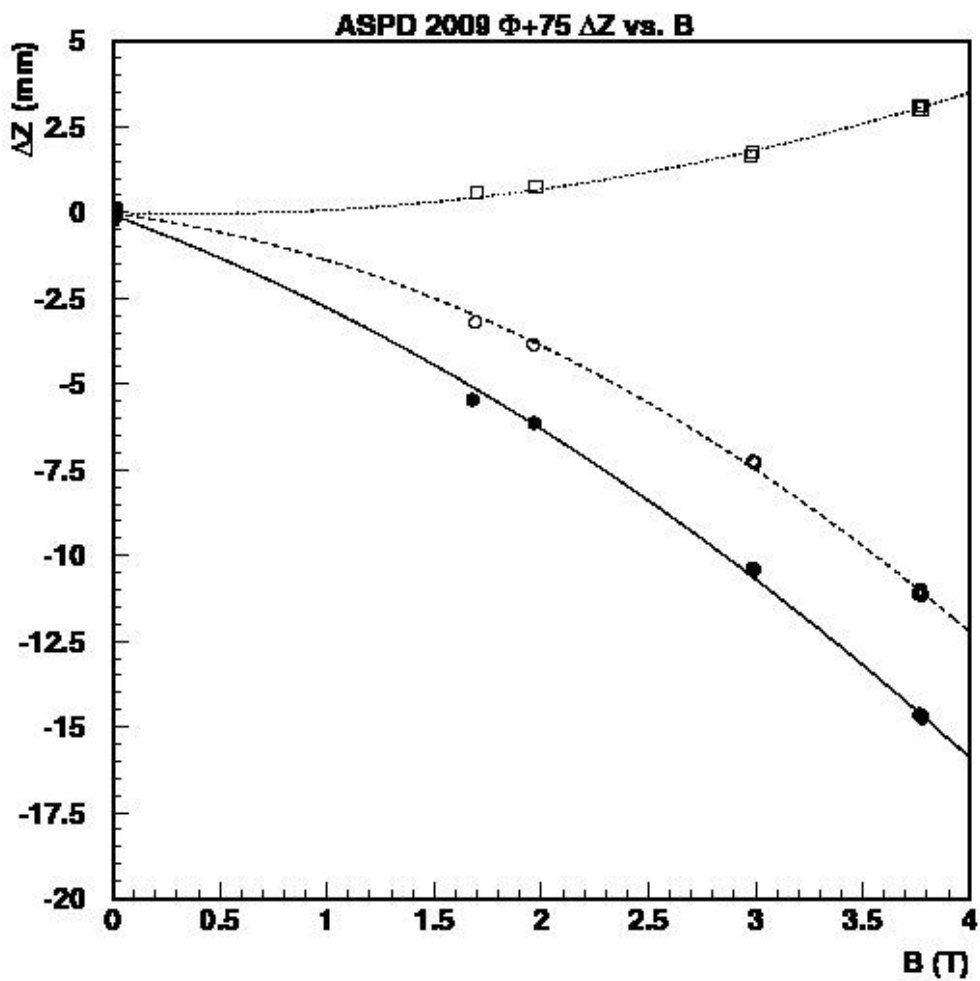


**Fig. 24:** During rump up in magnet intensity in 2009: motion  $\Delta Z$ (LD-AR) (dots),  $\Delta Z$ (LD&TP) with respect to the Interaction Point as seen from P2 in the laser path L2 (circles) and motion of ME/1/2 with respect to LD as seen from P5 in the laser path L4 (squares).

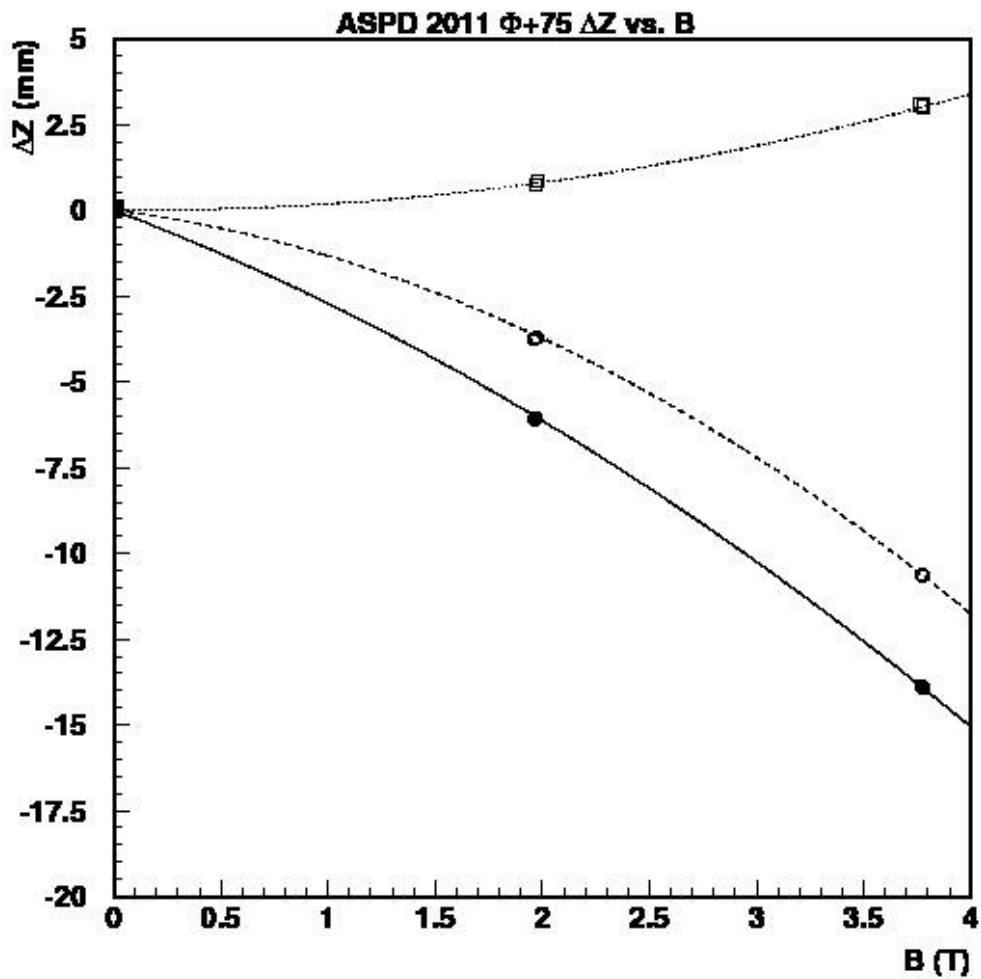


**Fig. 25:** During rump up in magnet intensity in 2011: motion  $\Delta Z(\text{LD-AR})$  (dots),  $\Delta Z(\text{LD\&TP})$  with respect to the Interaction Point as seen from P2 in the laser path L2 (circles) and motion of ME/1/2 with respect to LD as seen from P5 in the laser path L4 (squares).

**Table Captions**

**Table 1:** Average characteristics of the ASPD sensors for the CMS Alignment System.

**Table 2:** The ASPD construction parameters.

**Table 3:** Characteristics of the photo-sensors labelled P1, P2 and P3 at  $\Phi = +75^\circ$

**Table 4:** Characteristics of the photo-sensors labelled P4, P5 and P6 at  $\Phi = +75^\circ$

**Table 5:** Reconstruction resolutions (in  $\mu\text{m}$ ) of the ASPD sensors in the X ( $\sigma_x$ ) and Y ( $\sigma_y$ ) coordinates, for the units placed in the  $\Phi = 75^\circ$  quadrant at the + Z CMS side, in ideal conditions.

**Table 6:** The column contents are: Observed year, Magnet Cycle containing the SP inspected, Stability Period in question, working magnetic field intensity, switch off conditions and number of recorded data events from the ASPDs, respectively. The first data considered during a SP is the one taken 24 hours after the working magnetic field intensity

**Table 7:** For the light line L1, RMS of the distribution of the distance between the first data, in the stability period under study (see Table 6), and each of the other data points, in each of the crossed sensors by light path, during a given year of CMS operation. RMS quantities greater than  $300 \mu\text{m}$  are written in **bold**. When the RMS is greater than  $900 \mu\text{m}$  (more than  $3 \sigma$  away from stability) the amount is replaced by asterisks.

**Table 8:** For the light line L2, RMS of the distribution of the distance between the first data, in the stability period under study (see Table 6), and each of the other data points, in each of the crossed sensors by light path, during a given year of CMS operation. RMS quantities greater than  $300 \mu\text{m}$  are written in **bold**. When the RMS is greater than  $900 \mu\text{m}$  (more than  $3 \sigma$  away from stability) the amount is replaced by asterisks.

**Table 9:** For the light line L3, RMS of the distribution of the distance between the first data, in the stability period under study (see Table 6), and each of the other data points, in each of the crossed sensors by light path, during a given year of CMS operation. RMS quantities greater than  $300 \mu\text{m}$  are written in **bold**. When the RMS is greater than  $900 \mu\text{m}$  (more than  $3 \sigma$  away from stability) the amount is replaced by asterisks.

**Table 10:** For the light line L4, RMS of the distribution of the distance between the first data, in the stability period under study (see Table 6), and each of the other data points, in each of the crossed sensors by light path, during a given year of CMS operation. RMS quantities greater than  $300 \mu\text{m}$  are written in **bold**. When the RMS is greater than  $900 \mu\text{m}$  (more than  $3 \sigma$  away from stability) the amount is replaced by asterisks.

**Table 11:** The repositioning, or difference between the X and Y reconstructed coordinates at  $B = 0 \text{ T}$  before and after the Stability Period, in each of the three sensors in the Laser Path L1. Differences marked \*\*\*\* mean that at least one pair of point coordinates at  $B = 0 \text{ T}$  was missing. No ASPD data at  $B = 0 \text{ T}$  were recorded in the years 2013 and 2015.

**Table 12:** The repositioning, or difference between the X and Y reconstructed coordinates at  $B = 0 \text{ T}$  before and after the Stability Period, in each of the three sensors in the Laser Path L2. Differences marked \*\*\*\* mean that at least one pair of point coordinates at  $B = 0 \text{ T}$  was missing. No ASPD data at  $B = 0 \text{ T}$  were recorded in the years 2013 and 2015.

**Table 13:** The repositioning, or difference between the X and Y reconstructed coordinates at  $B = 0$  T before and after the Stability Period, in each of the three sensors in the Laser Path L3. Differences marked \*\*\*\* mean that at least one pair of point coordinates at  $B = 0$  T was missing. No ASPD data at  $B = 0$  T were recorded in the years 2013 and 2015.

**Table 14:** The repositioning, or difference between the X and Y reconstructed coordinates at  $B = 0$  T before and after the Stability Period, in each of the three sensors in the Laser Path L4. Differences marked \*\*\*\* mean that at least one pair of point coordinates at  $B = 0$  T was missing. No ASPD data at  $B = 0$  T were recorded in the years 2013 and 2015.

**Table 15:** The largest displacement, or difference between the X and Y reconstructed coordinates at  $B = 3.8$  T at the beginning of the Stability Period and the ones reconstructed at  $B = 0$  T before the ramping up in magnetic field intensity, for each of the three sensors in the Laser Path L1. Differences marked \*\*\*\* mean that at least one pair of point coordinates at  $B = 0$  T or  $B = 3.8$  T was missing. No ASPD data at  $B = 0$  T were recorded in the years 2013 and 2015.

**Table 16:** The largest displacement, or difference between the X and Y reconstructed coordinates at  $B = 3.8$  T at the beginning of the Stability Period and the ones reconstructed at  $B = 0$  T before the ramping up in magnetic field intensity, for each of the three sensors in the Laser Path L2. Differences marked \*\*\*\* mean that at least one pair of point coordinates at  $B = 0$  T or  $B = 3.8$  T was missing. No ASPD data at  $B = 0$  T were recorded in the years 2013 and 2015.

**Table 17:** The largest displacement, or difference between the X and Y reconstructed coordinates at  $B = 3.8$  T at the beginning of the Stability Period and the ones reconstructed at  $B = 0$  T before the ramping up in magnetic field intensity, for each of the three sensors in the Laser Path L4. Differences marked \*\*\*\* mean that at least one pair of point coordinates at  $B = 0$  T or  $B = 3.8$  T was missing. No ASPD data at  $B = 0$  T were recorded in the years 2013 and 2015.

**Table 18:** Fitted parameters for the quadratic functions in Figs. 23 to 25, for the years 2008, 2009 and 2011, respectively. In the fits, the used error for  $\Delta Z$  was  $40 \mu\text{m}$  (the Sakae potentiometer resolution). For  $\Delta Y_d$  they were taken from Table 5.

Sensitivity (mA/W)	$16.3 \pm 7.6$
$\sigma_x$ ( $\mu\text{m}$ )	$5.2 \pm 2.6$
$\sigma_y$ ( $\mu\text{m}$ )	$5.1 \pm 2.4$
$\Theta_x$ ( $\mu\text{rad}$ )	$-1.1 \pm 5.1$
$\Theta_y$ ( $\mu\text{rad}$ )	$0.8 \pm 3.8$
Transmittance (%)	$84.8 \pm 2.9$

**Table 1:** Average characteristics of the ASPD sensors for the CMS Alignment System.

a-SiC:H thickness	195 nm
Strip thickness	110 nm
Glass thickness	1 mm
Active area	$28 \times 28 \text{ mm}^2$
Number of strips	64 horizontal + 64 vertical
Strip pitch	430 $\mu\text{m}$
Strip gap	22 $\mu\text{m}$

**Table 2:** The ASPD construction parameters.

Label	Characteristics	Active Face	Glass Face
P1	$\Theta_x$ [ $\mu\text{rad}$ ]	$3.2 \pm 1.9$	$3.7 \pm 2.9$
	$\Theta_y$ [ $\mu\text{rad}$ ]	$2.2 \pm 2.1$	$0.2 \pm 4.9$
	Transmittance (%)	$86 \pm 1$	$84 \pm 2$
	$\sigma_x$ [ $\mu\text{m}$ ]	7.4	8.7
	$\sigma_y$ [ $\mu\text{m}$ ]	5.4	11.3
P2	$\Theta_x$ [ $\mu\text{rad}$ ]	$2.9 \pm 4.3$	$1.4 \pm 4.1$
	$\Theta_y$ [ $\mu\text{rad}$ ]	$4.0 \pm 3.7$	$-2.5 \pm 3.1$
	Transmittance (%)	$86 \pm 1$	$85 \pm 1$
	$\sigma_x$ [ $\mu\text{m}$ ]	4.8	6.7
	$\sigma_y$ [ $\mu\text{m}$ ]	4.2	7.5
P3	$\Theta_x$ [ $\mu\text{rad}$ ]	$-3.0 \pm 5.7$	$-2.9 \pm 3.2$
	$\Theta_y$ [ $\mu\text{rad}$ ]	$6.8 \pm 5.2$	$-4.3 \pm 7.1$
	Transmittance (%)	$85 \pm 2$	$85 \pm 1$
	$\sigma_x$ [ $\mu\text{m}$ ]	5.9	7.0
	$\sigma_y$ [ $\mu\text{m}$ ]	4.4	4.4

**Table 3:** Characteristics of the photo-sensors labelled P1, P2 and P3 at  $\Phi = + 75^\circ$

Label	Characteristic	Active Face	Glass Face
P4	$\Theta_x$ [ $\mu\text{rad}$ ]	$-3.7 \pm 3.5$	$-5.0 \pm 3.7$
	$\Theta_y$ [ $\mu\text{rad}$ ]	$2.8 \pm 4.4$	$0.1 \pm 2.7$
	Transmittance (%)	$85 \pm 1$	$85 \pm 1$
	$\sigma_x$ [ $\mu\text{m}$ ]	6.4	6.3
	$\sigma_y$ [ $\mu\text{m}$ ]	2.9	4.4
P5	$\Theta_x$ [ $\mu\text{rad}$ ]	$-5.2 \pm 1.7$	$-6.4 \pm 2.0$
	$\Theta_y$ [ $\mu\text{rad}$ ]	$0.1 \pm 2.0$	$1.4 \pm 2.0$
	Transmittance (%)	$76 \pm 3$	$76 \pm 3$
	$\sigma_x$ [ $\mu\text{m}$ ]	6.9	6.2
	$\sigma_y$ [ $\mu\text{m}$ ]	3.2	3.0
P6	$\Theta_x$ [ $\mu\text{rad}$ ]	$-5.1 \pm 3.4$	$-5.8 \pm 3.1$
	$\Theta_y$ [ $\mu\text{rad}$ ]	$4.6 \pm 3.3$	$-3.6 \pm 9.4$
	Transmittance (%)	$86 \pm 1$	$85 \pm 1$
	$\sigma_x$ [ $\mu\text{m}$ ]	6.7	7.4
	$\sigma_y$ [ $\mu\text{m}$ ]	2.8	4.4

**Table 4:** Characteristics of the photo-sensors labelled P4, P5 and P6 at  $\Phi = + 75^\circ$

Sensor Resolutions	P1 $\sigma_x/\sigma_y$	P2 $\sigma_x/\sigma_y$	P3 $\sigma_x/\sigma_y$	P4 $\sigma_x/\sigma_y$	P5 $\sigma_x/\sigma_y$	P6 $\sigma_x/\sigma_y$
Light Path 1	10.0/7.4	10.5/19.5	7.0/4.4			
Light Path 2	8.7/11.3	6.8/9.1	12.4/10.4			
Light Path 3	8.7/11.3	6.8/9.1	12.4/10.4			
Light Path 4				6.3/4.4	6.9/3.2	7.3/4.5

**Table 5:** Reconstruction resolutions (in  $\mu\text{m}$ ) of the ASPD sensors in the X ( $\sigma_x$ ) and Y ( $\sigma_y$ ) coordinates, for the units placed in the  $\Phi = 75^\circ$  quadrant at the + Z CMS side, in ideal conditions.

Year	Magnet Cycle nb. From Ref. [8]	SP nb. From Ref. [8]	$B_{\text{max}}$ [T]	Switch off cond.	Total number of recorded ASPD events
2008	5	1	3.8	Controlled	23
2009	14	6	3.8	Controlled	15
2010	4	1	3.8	Fast Dump	44
2011	3	2	3.8	Fast Dump	46
2012	2	2	3.8	Fast Dump	187
2013	1	1	3.8	Fast Dump	64
2015	4	1	3.8	Fast Dump	30

**Table 6:** The column contents are: Observed year, Magnet Cycle containing the SP inspected, Stability Period in question, working magnetic field intensity, switch off conditions and number of recorded data events from the ASPDs, respectively. The first data considered during a SP is the one taken 24 hours after the working magnetic field intensity is reached.

Light Line L1	Sensor P3	Sensor P2	Sensor P1
Year	RMS ( $\mu\text{m}$ )	RMS ( $\mu\text{m}$ )	RMS ( $\mu\text{m}$ )
2008	0.5	12.5	11.0
2009	0.9	10.9	<b>447.1</b>
2010	0.9	72.7	74.8
2011	1.6	44.6	49.9
2012	****	****	****
2013	1.9	10.8	17.8
2015	****	8.3	<b>588.9</b>

**Table 7:** For the light line L1, RMS of the distribution of the distance between the first data, in the stability period under study (see Table 6), and each of the other data points, in each of the crossed sensors by light path, during a given year of CMS operation. RMS quantities greater than  $300 \mu\text{m}$  are written in **bold**. When the RMS is greater than  $900 \mu\text{m}$  (more than  $3 \sigma$  away from stability) the amount is replaced by asterisks.

Light Line L2	Sensor P1	Sensor P2	Sensor P3
Year	RMS ( $\mu\text{m}$ )	RMS ( $\mu\text{m}$ )	RMS ( $\mu\text{m}$ )
2008	44.5	81.3	164.3
2009	35.7	<b>423.2</b>	<b>446.1</b>
2010	18.7	54.7	68.9
2011	52.2	46.8	82.3
2012	<b>766.8</b>	****	****
2013	20.7	33.8	54.0
2015	11.8	17.6	27.7

**Table 8:** For the light line L2, RMS of the distribution of the distance between the first data, in the stability period under study (see Table 6), and each of the other data points, in each of the crossed sensors by light path, during a given year of CMS operation. RMS quantities greater than  $300 \mu\text{m}$  are written in **bold**. When the RMS is greater than  $900 \mu\text{m}$  (more than  $3 \sigma$  away from stability) the amount is replaced by asterisks.

Light Line L3	Sensor P1	Sensor P2	Sensor P3
Year	RMS ( $\mu\text{m}$ )	RMS ( $\mu\text{m}$ )	RMS ( $\mu\text{m}$ )
2008	207.3	196.1	218.3
2009	112.5	<b>568.0</b>	<b>615.9</b>
2010	<b>348.1</b>	223.3	****
2011	260.3	260.5	****
2012	****	<b>819.1</b>	****
2013	99.3	160.8	****
2015	****	52.0	****

**Table 9:** For the light line L3, RMS of the distribution of the distance between the first data, in the stability period under study (see Table 6), and each of the other data points, in each of the crossed sensors by light path, during a given year of CMS operation. RMS quantities greater than  $300 \mu\text{m}$  are written in **bold**. When the RMS is greater than  $900 \mu\text{m}$  (more than  $3 \sigma$  away from stability) the amount is replaced by asterisks.

Light Line L4	Sensor P4	Sensor P5	Sensor P6
Year	RMS ( $\mu\text{m}$ )	RMS ( $\mu\text{m}$ )	RMS ( $\mu\text{m}$ )
2008	33.2	41.0	71.5
2009	129.2	161.4	<b>373.9</b>
2010	104.9	17.6	26.6
2011	51.7	55.7	72.3
2012	<b>621.0</b>	****	74.6
2013	****	23.1	37.0
2015	****	****	22.5

**Table 10:** For the light line L4, RMS of the distribution of the distance between the first data, in the stability period under study (see Table 6), and each of the other data points, in each of the crossed sensors by light path, during a given year of CMS operation. RMS quantities greater than  $300 \mu\text{m}$  are written in **bold**. When the RMS is greater than  $900 \mu\text{m}$  (more than  $3 \sigma$  away from stability) the amount is replaced by asterisks.

ASPD	P3		P2		P1	
Year	$\Delta X_r[\mu\text{m}]$	$\Delta Y_r[\mu\text{m}]$	$\Delta X_r[\mu\text{m}]$	$\Delta Y_r[\mu\text{m}]$	$\Delta X_r[\mu\text{m}]$	$\Delta Y_r[\mu\text{m}]$
2008	1	3	-40	79	-35	-98
2009	1	5	25	-27	13	-174
2010	-57	85	****	****	-36	-104
2011	1	-1	-2	-5	-39	-38
2012	1	-13	-57	121	<b>513</b>	****

**Table 11:** The repositioning, or difference between the X and Y reconstructed coordinates at  $B = 0$  T before and after the Stability Period, in each of the three sensors in the Laser Path L1. Differences marked \*\*\*\* mean that at least one pair of point coordinates at  $B = 0$  T was missing. No ASPD data at  $B = 0$  T were recorded in the years 2013 and 2015.

ASPD	P1		P2		P3	
Year	$\Delta X_r[\mu\text{m}]$	$\Delta Y_r[\mu\text{m}]$	$\Delta X_r[\mu\text{m}]$	$\Delta Y_r[\mu\text{m}]$	$\Delta X_r[\mu\text{m}]$	$\Delta Y_r[\mu\text{m}]$
2008	-29	-23	-31	11	183	1
2009	-23	17	-70	-189	-146	-167
2010	-8	101	****	****	****	****
2011	51	127	105	1	-51	1
2012	-74	-150	-103	****	85	1

**Table 12:** The repositioning, or difference between the X and Y reconstructed coordinates at  $B = 0$  T before and after the Stability Period, in each of the three sensors in the Laser Path L2. Differences marked \*\*\*\* mean that at least one pair of point coordinates at  $B = 0$  T was missing. No ASPD data at  $B = 0$  T were recorded in the years 2013 and 2015.

ASPD	P1		P2		P3	
Year	$\Delta X_r[\mu\text{m}]$	$\Delta Y_r[\mu\text{m}]$	$\Delta X_r[\mu\text{m}]$	$\Delta Y_r[\mu\text{m}]$	$\Delta X_r[\mu\text{m}]$	$\Delta Y_r[\mu\text{m}]$
2008	-232	<b>927</b>	<b>-526</b>	1	****	<b>-1156</b>
2009	-88	160	-154	****	-386	****
2010	<b>474</b>	39	****	****	****	****
2011	<b>438</b>	****	<b>514</b>	****	****	****
2012	<b>973</b>	****	1281	****	****	****

**Table 13:** The repositioning, or difference between the X and Y reconstructed coordinates at  $B = 0$  T before and after the Stability Period, in each of the three sensors in the Laser Path L3. Differences marked \*\*\*\* mean that at least one pair of point coordinates at  $B = 0$  T was missing. No ASPD data at  $B = 0$  T were recorded in the years 2013 and 2015.

ASPD	P4		P5		P6	
Year	$\Delta X_r[\mu\text{m}]$	$\Delta Y_r[\mu\text{m}]$	$\Delta X_r[\mu\text{m}]$	$\Delta Y_r[\mu\text{m}]$	$\Delta X_r[\mu\text{m}]$	$\Delta Y_r[\mu\text{m}]$
2008	-36	3	50	-46	58	-257
2009	35	32	26	34	9	98
2010	11	116	-4	128	-2	1
2011	-35	168	-53	153	-121	1
2012	<b>-453</b>	-104	82	<b>-655</b>	248	****

**Table 14:** The repositioning, or difference between the X and Y reconstructed coordinates at  $B = 0$  T before and after the Stability Period, in each of the three sensors in the Laser Path L4. Differences marked \*\*\*\* mean that at least one pair of point coordinates at  $B = 0$  T was missing. No ASPD data at  $B = 0$  T were recorded in the years 2013 and 2015.

ASPD	P3		P2		P1	
Year	$\Delta X_d$ [mm]	$\Delta Y_d$ [mm]	$\Delta X_d$ [mm]	$\Delta Y_d$ [mm]	$\Delta X_d$ [mm]	$\Delta Y_d$ [mm]
2008	0.001	0.002	-0.017	0.121	-0.288	-11.862
2009	-0.002	0.001	0.008	-0.347	-0.038	-9.982
2010	-0.001	0.001	****	****	-0.654	-10.301
2011	0.001	0.001	-0.018	-0.449	-0.675	-10.439
2012	0.001	-0.003	-0.036	-0.437	-0.111	-7.074

**Table 15:** The largest displacement, or difference between the X and Y reconstructed coordinates at  $B = 3.8 T$  at the beginning of the Stability Period and the ones reconstructed at  $B = 0 T$  before the ramping up in magnetic field intensity, for each of the three sensors in the Laser Path L1. Differences marked \*\*\*\* mean that at least one pair of point coordinates at  $B = 0 T$  or  $B = 3.8 T$  was missing. No ASPD data at  $B = 0 T$  were recorded in the years 2013 and 2015.

ASPD	P1		P2		P3	
Year	$\Delta X_d$ [mm]	$\Delta Y_d$ [mm]	$\Delta X_d$ [mm]	$\Delta Y_d$ [mm]	$\Delta X_d$ [mm]	$\Delta Y_d$ [mm]
2008	0.051	0.378	0.424	-11.293	0.554	****
2009	0.057	0.239	0.312	-9.850	0.514	-8.341
2010	0.084	0.308	0.367	****	0.337	****
2011	0.054	0.120	0.295	****	****	****
2012	-0.018	-0.067	0.131	-7.023	0.050	****

**Table 16:** The largest displacement, or difference between the X and Y reconstructed coordinates at  $B = 3.8 T$  at the beginning of the Stability Period and the ones reconstructed at  $B = 0 T$  before the ramping up in magnetic field intensity, for each of the three sensors in the Laser Path L2. Differences marked \*\*\*\* mean that at least one pair of point coordinates at  $B = 0 T$  or  $B = 3.8 T$  was missing. No ASPD data at  $B = 0 T$  were recorded in the years 2013 and 2015.

ASPD	P4		P5		P6	
Year	$\Delta X_d$ [mm]	$\Delta Y_d$ [mm]	$\Delta X_d$ [mm]	$\Delta Y_d$ [mm]	$\Delta X_d$ [mm]	$\Delta Y_d$ [mm]
2008	0.101	0.455	0.135	3.151	-0.177	7.791
2009	0.006	0.262	0.191	2.560	0.066	7.712
2010	-0.106	0.369	0.100	3.184	-0.169	****
2011	-0.107	0.199	0.100	3.016	-0.127	****
2012	-0.447	-0.009	0.145	2.267	0.091	5.844

**Table 17:** The largest displacement, or difference between the  $X$  and  $Y$  reconstructed coordinates at  $B = 3.8$  T at the beginning of the Stability Period and the ones reconstructed at  $B = 0$  T before the ramping up in magnetic field intensity, for each of the three sensors in the Laser Path L4. Differences marked \*\*\*\* mean that at least one pair of point coordinates at  $B = 0$  T or  $B = 3.8$  T was missing. No ASPD data at  $B = 0$  T were recorded in the years 2013 and 2015.

	a [mm/T <sup>2</sup> ]	b [mm/T]	c [mm]	$\chi^2$ /NDF
$\Delta Z$ (LD-AR) 2008	-0.469±0.006	-2.218±0.026	-0.018±0.023	78/17
2009	-0.418±0.008	-2.285±0.029	-0.080±0.016	172/14
2011	-0.350±0.009	-2.369±0.034	0.004±0.020	1/6
$\Delta Y_d$ (P2-L2) 2008	-0.596±0.002	-0.788±0.007	0.012±0.004	614/9
2009	-0.560±0.001	-0.810±0.005	-0.028±0.003	2025/14
2011	-0.537±0.002	-0.790±0.006	-0.001±0.004	24/6
$\Delta Y_d$ (P5-L4) 2008	0.330±0.001	-0.351±0.002	-0.005±0.002	381/11
2009	0.269±0.001	-0.205±0.002	0.006±0.001	2100/14
2011	0.224±0.016	-0.051±0.006	0.016±0.004	10/6

**Table 18:** Fitted parameters for the quadratic functions in Figs. 23 to 25, for the years 2008, 2009 and 2011, respectively. In the fits, the used error for  $\Delta Z$  was 40  $\mu$ m (the Sakae potentiometer resolution). For  $\Delta Y_d$  they were taken from Table 5.